



Live imaging of airway epithelium reveals that mucociliary clearance modulates SARS-CoV-2 spread

Received: 21 August 2023

Accepted: 20 October 2024

Published online: 02 November 2024

Check for updates

Mark E. Becker¹, Laura Martin-Sancho², Lacy M. Simons¹, Michael D. McRaven¹, Sumit K. Chanda¹, Judd F. Hultquist¹ & Thomas J. Hope¹✉

SARS-CoV-2 initiates infection in the conducting airways, where mucociliary clearance inhibits pathogen penetration. However, it is unclear how mucociliary clearance impacts SARS-CoV-2 spread after infection is established. To investigate viral spread at this site, we perform live imaging of SARS-CoV-2 infected differentiated primary human bronchial epithelium cultures for up to 12 days. Using a fluorescent reporter virus and markers for cilia and mucus, we longitudinally monitor mucus motion, ciliary motion, and infection. Infected cell numbers peak at 4 days post infection, forming characteristic foci that tracked mucus movement. Inhibition of MCC using physical and genetic perturbations limits foci. Later in infection, mucociliary clearance deteriorates. Increased mucus secretion accompanies ciliary motion defects, but mucociliary clearance and vectorial infection spread resume after mucus removal, suggesting that mucus secretion may mediate MCC deterioration. Our work shows that while MCC can facilitate SARS-CoV-2 spread after initial infection, subsequent MCC decreases inhibit spread, revealing a complex interplay between SARS-CoV-2 and MCC.

SARS-CoV-2, the causative agent of COVID-19, continues to circulate widely following its emergence in 2019. In most cases, the first site of SARS-CoV-2 infection is the conducting airways^{1–3}. These sections of the airway are lined with a pseudostratified epithelium blanketed in mucus, which is produced by goblet and other secretory cells. The mucus acts as a barrier between the environment and the epithelium, trapping particulate matter including pathogens. Multiciliated cells lining the airway move the mucus away from the respiratory airways and toward the pharynx, keeping the airways patent and thereby permitting gas exchange at alveolar surfaces. This process of mucociliary clearance (MCC) is a key innate immune barrier; defects in MCC as seen in primary ciliary dyskinesia and cystic fibrosis are associated with increased frequency and severity of respiratory infections⁴.

While MCC inhibits initial infection, its role in viral spread following the establishment of an infection is less clear. If virions are shed from the apical surface of infected epithelial cells, MCC may facilitate spread. For example, Respiratory Syncytial Virus (RSV) has been found to form cometlike foci in model systems with functional MCC, suggesting its spread may be facilitated by mucociliary movement⁵. MCC has been considered in silico modeling of early stages of intra-host SARS-CoV-2 and influenza A virus (IAV) spread, but limited experimental data on the impact of MCC on early spread of these viruses is available^{6,7}. Wu et al. show that SARS-CoV-2 relies on many aspects of cilia biology over its replicative cycle, including a dependence on MCC for local spread, but questions remain as to the timing, magnitude, and variability of this effect⁸.

¹Department of Cell & Developmental Biology, Feinberg School of Medicine, Northwestern University, Chicago, IL, USA. ²Department of Infectious Diseases, Imperial College London, London, UK. ³Division of Infectious Diseases, Feinberg School of Medicine, Northwestern University, Chicago, IL, USA. ⁴Department of Immunology and Microbiology, Scripps Research Institute, La Jolla, CA, USA. ✉e-mail: thope@northwestern.edu

MCC is a complex, dynamic system, with feedback mechanisms between mucus composition, periciliary liquid composition, and ciliary motion patterns that ultimately determine the physicochemical properties of the mucus and its movement⁹. Viral infection can induce changes in MCC, both through the direct modulation of infected cell function as well as indirectly through the induction of innate immune and inflammatory signaling pathways^{10–12}. Impaired multiciliated cell function and death of multiciliated cells are thought to be major mechanisms of SARS-CoV-2's impact on MCC, as these cells are the primary target for SARS-CoV-2 infection in the airway^{11,13–16}. SARS-CoV-2 infection is also known to increase mucus secretion^{11,17,18}. However, the details of how and when MCC changes during infection remain unclear.

Primary human bronchial epithelial cells (HBEs) grown at an air-liquid interface (ALI) support MCC and are commonly used to model the airway in studies of infectious disease^{19–27}. However, fixed time-point imaging of these cultures has resulted in a limited understanding of MCC dynamics, particularly given the heterogeneity of ALI cultures. Here, we use live imaging of SARS-CoV-2 infected ALI cultures to track mucus motion, ciliary motion, and viral spread^{1,28}. We find that MCC, though an efficient barrier to initial infection, appears to facilitate the spread of SARS-CoV-2 in the first days of infection. Later in infection, a

combination of multiciliated cell depletion and mucus secretion limit MCC. These results suggest a complicated interplay between the host MCC system and respiratory virus infection.

Results

Inverted air-liquid interface cultures support live imaging of SARS-CoV-2 infection and mucociliary clearance

To model the human airway in a format amenable to live imaging, we used an inverted primary human bronchial epithelium air-liquid interface (ALI) culture system following the method of Zaderer et al. (Fig. 1a)²⁸. Briefly, primary HBEs were seeded on the underside of permeable transwell supports to enable high-resolution live imaging of the apical surface of the cells. After differentiation, these cultures developed a characteristic pseudostratified morphology resembling human bronchial epithelium with multiciliated cells and goblet cells as confirmed by immunostaining for markers of cell-cell junctions (actin (phalloidin)), cilia (acetyl α -tubulin), and mucus (MUC5AC) (Fig. 1b). While these largely formed a monolayer on the support, most ALI cultures contained at least a few furrows and intraepithelial lumens henceforth referred to as crypts (Supplementary Fig. 1a). These are an artifact of ALI culture and do not occur *in vivo* in the airway. However, crypt-bearing cultures still displayed ciliation and mucus production

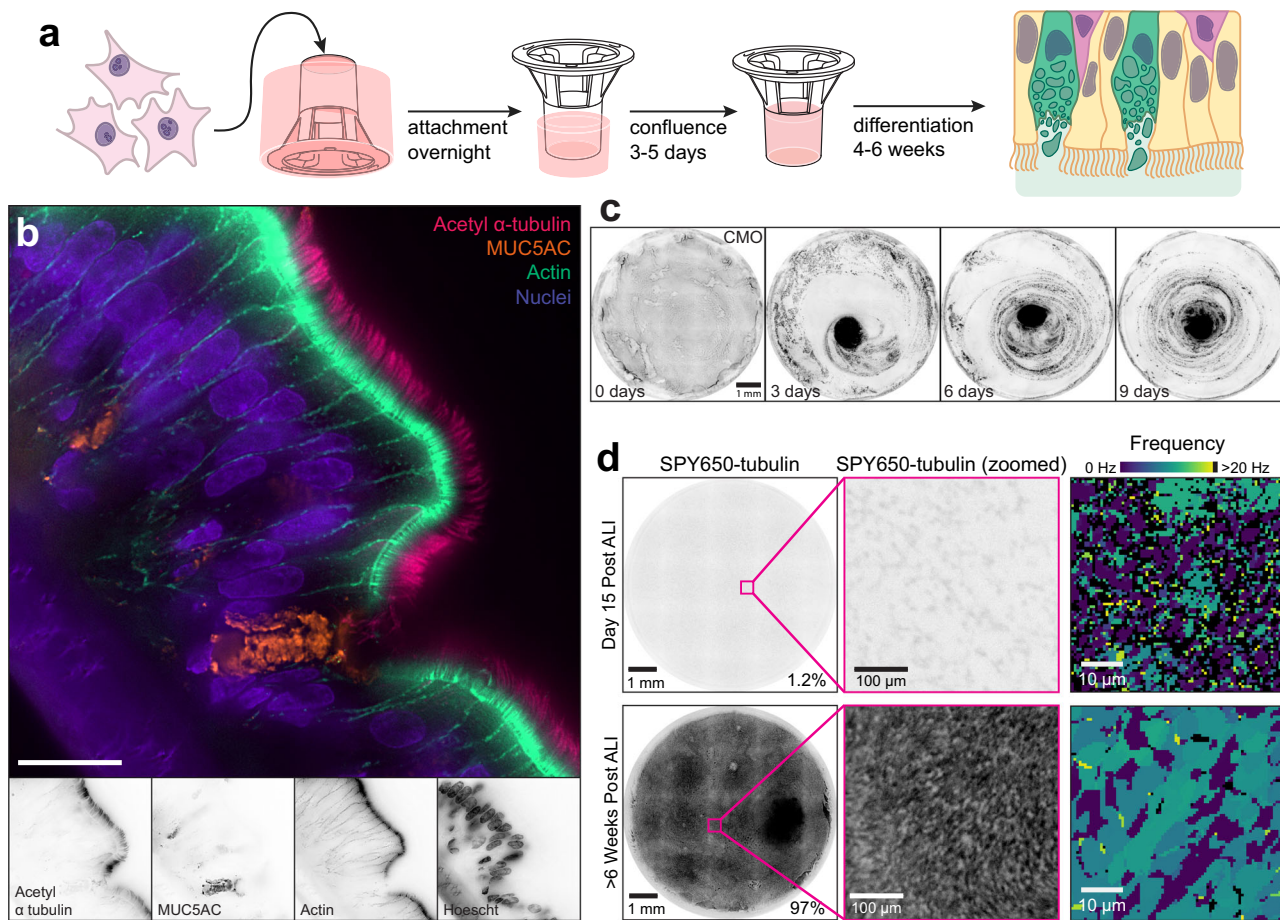


Fig. 1 | Inverted ALI culture models support MCC. **a** A schematic of inverted ALI culture. **b** Representative immunofluorescent image of a section of a differentiated ALI culture stained for: cilia (acetyl α -tubulin, bright pink), cell-cell junctions (actin (phalloidin), spring green) mucus (MUC5AC, amber), and nuclei (Hoescht, electric indigo). Below, single channels in inverted grayscale. Scale bar = 20 μ m. Staining was repeated for cultures from 9 donors with comparable results. **c** Time-lapse of an inverted ALI culture incubated with CellMask Orange Plasma Membrane stain (CMO, inverted greyscale) demonstrating rotary mucociliary clearance over 9 days. Scale bar = 1 mm. **d** SPY650-tubulin signal in immature and mature ALI cultures. Left

panels are images of whole cultures at different stages with SPY-650 tubulin in inverted grayscale, with zoomed field of view outlined in pink. Right panels are the frequency of SPY650-tubulin signal in high-speed videos of fields of view of the cultures shown in the left panels. Frequency is shown using the viridis colormap, with high-frequency noisy pixels in black. Scale bar for whole cultures is 1 mm; for insets 100 μ m; for frequency 10 μ m. Comparable results for differentiated cultures were observed across at least 5 experiments and 6 donors. Undifferentiated results were typical for 2 cultures.

both on the surface and within the lumens, analogous to the interior lumens of organoid models. Donors differ in their propensity to form these structures, as previously observed²⁹.

To track the motion of mucus on the apical surface, we stained live cultures with either CellMask Orange Plasma Membrane (CMO) or NucView 530 (NV). CMO labels the plasma membrane upon application to the apical surface, but after 1–2 h, it accumulates in shed cells and presumptive membrane debris in the mucus (Supplementary Video 1). This dye continues to label the apical surface at a lower intensity, sometimes requiring careful inspection of Z-stacks to distinguish cell motion from mucus motion. Later experiments were performed with NV, a fluorogenic caspase 3/7 substrate, which has somewhat less cellular localization. NV labels apoptotic cells, which are shed into the mucus allowing persistent monitoring of MCC (Supplementary Video 2). These dyes mark mucus motion comparably to fluorescent plastic beads, though cellular background complicates computational analysis (Supplementary Videos 3, 4). The apical mucus disc in inverted ALI cultures often rotated over time, indicative of coordinated MCC (Fig. 1c). Where rotary MCC was not present, the mucus flowed in a disorganized manner consistent with uncoordinated patches of locally coordinated multiciliated cells (Supplementary Videos 1, 2)³⁰. Crypt-bearing cultures sometimes showed rotary MCC despite the alterations to surface structure (Supplementary Video 5). Due to heterogeneity in MCC across the culture surface and technical limitations of our imaging regime including low framerate relative to MCC speed, we relied on manual classification of MCC pattern as disorganized or rotary rather than particle tracking to quantify mucus speed. *In vivo*, coordinated MCC continually moves mucus toward the pharynx rather than recirculating it over the epithelium. This is a limitation of the geometry of the transwell-based ALI culture system.

To observe multiciliated cells, we stained live cultures with SPY650-tubulin (Supplementary Video 6). All differentiated cultures had SPY650-tubulin signal intensity consistent with ciliated cells covering most of the apical surface, with a median coverage of 83% (Fig. 1d). SPY650-tubulin also labels cilia with sufficient intensity to acquire high framerate movies of ciliary motion and determine ciliary beat frequency (Fig. 1d right, Supplementary Video 6). The median beat frequency observed was 9 Hz, slightly slower than expected. Over non-beating regions, uniformly distributed noise up to 62.5 Hz (1/2 video framerate) was observed; we color such high-frequency pixels black in visualizations to facilitate interpretation. The limited exposure time of such movies results in a poor signal-to-noise ratio. To improve both visualization and analysis, we denoised the movies using Cellpose 3 (Supplementary Fig. 2)³¹.

Though epithelial cells are densely packed and immotile in homeostatic conditions, imaging cultures with SPY650-tubulin occasionally revealed collective cell migration resembling epithelial unjamming (Supplementary Video 7)³². In unjamming, the solid-like jammed epithelial cell collective becomes migratory with a fluid-like motion while retaining epithelial features such as cell-cell junctions. This migration led to the formation and dissolution of densely ciliated furrows, visible as bright structures in SPY650-tubulin staining (Supplementary Video 7, Supplementary Fig. 1b, c). Cysts (smaller crypts, either blind or with a pore) did not appear to be associated with cell migration. Of 124 cultures, 4 had patchy ciliation with a hypermobile phenotype; 54 had widespread though not global migration; 38 had cell migration restricted to the rim; and 28 were well-jammed. Cultures with widespread cell migration were significantly more likely to contain furrow-type crypts ($\chi^2 = 89$, $df = 6$, $p < 2.2 \times 10^{-16}$) and to have disorganized mucus motion ($\chi^2 = 25$, $df = 3$, $p = 1.1 \times 10^{-5}$) (Supplementary Fig. 3). Fully differentiated ALI cultures should consist of jammed, non-migratory epithelia, as seen in healthy tissue *in vivo*. Epithelial unjamming occurs in development, in wound repair, and in disease processes including asthma and idiopathic pulmonary

fibrosis^{33–36}. Differentiated ALI cultures with extensive cell migration may resemble these states rather than healthy tissue. Taken together, these data indicate that the inverted ALI culture model resembles human bronchial epithelium and supports MCC for live imaging, though care must be taken to screen and control for tissue culture artifacts. Similar care must be taken in extrapolating observations of the restricted MCC in this model to the unidirectional MCC *in vivo*.

Immunostaining of inverted ALI cultures for ACE2 (the SARS-CoV-2 receptor) and TMPRSS2 (the major protease cofactor) confirmed that these cells express both factors required for SARS-CoV-2 entry at the apical surface of the epithelium and among the cilia, among other sites (Fig. 2a, b). To assess the permissivity of these cultures to SARS-CoV-2 infection, we inoculated inverted and conventionally-grown ALI cultures with SARS-CoV-2 USA/WA1-2020 at a multiplicity of infection (MOI) of 1 via the apical surface, then quantified viral nucleocapsid (N) RNA in apical rinsates (mucus eluted in PBS) over time by quantitative PCR (qPCR) (Fig. 2c). To avoid disturbing replication kinetics, each infected culture was only used for one rinsate timepoint. At no time point did N titers significantly differ between inverted and conventionally-grown ALI cultures. The concentration of N RNA in the mucus increased over time, consistent with productive viral replication and release from the apical surface. Maximum N concentration was observed at 168 h post-infection (HPI) at 2.3×10^8 N copies per square millimeter of culture surface area, though the increase in N concentration slowed after 72 HPI.

To further confirm permissivity, we infected differentiated ALI cultures with SARS-CoV-2 as above and stained for viral replication compartments with anti-double-stranded RNA (dsRNA) antibodies or for viral antigens with anti-N or anti-Spike (S) antibodies at 72 HPI (Fig. 2d). Each marker of infection was detectable above background and displayed distinct localization patterns within the epithelium. S primarily localized both around the nucleus and at the apical surface of the cells below the cilia (Fig. 2e). N localized within the cytoplasm with occasional staining in the cilia. dsRNA occurred apical of the nucleus. Dimmer puncta of co-localized S and N occur within the cilia & mucus layer (Fig. 2f, insets). Punctate protein antigen staining did not necessarily co-localize with dsRNA, suggesting that at least some of the puncta may represent actual virions rather than autofluorescent or noninfectious debris (Fig. 2f). If virions are released into mucus, that suggests that MCC could be relevant for viral particle spread within the airway. Inverted ALI cultures are thus a suitable model for studying early SARS-CoV-2 spread in the context of mucociliary clearance.

Live imaging of inverted ALI cultures reveals kinetics and spatial aspects of SARS-CoV-2 spread

To characterize SARS-CoV-2 spread locally within the bronchial epithelium, we performed live imaging of inverted ALI cultures after infection with a SARS-CoV-2 USA/WA1-2020 derived fluorescent reporter virus that has eGFP inserted into the ORF7a locus (icSARS-CoV-2/d7a-eGFP)³. Infected cells become fluorescent as GFP is expressed. Differentiated ALI cultures from 9 donors were infected in at least technical triplicate and imaged longitudinally for up to 12 days post-infection. Using CMO to simultaneously track MCC, we observed that most cultures had comet-like foci of infection that closely followed the tracks of the mucus disks (Fig. 3a, Supplementary Video 8). When visualized by temporal color code (Fig. 3a, right panel), in which successive frames of single channels of a video are re-colored and projected to permit inference of motion³⁷, the motion of the mucus (yellow and green) was observed to precede the development of infection foci (cyan). Similar results were obtained when using NV to track MCC and SPY650-tubulin to monitor the epithelium (Supplementary Video 9, Supplementary Fig. 4).

To quantify infection kinetics, we approximated the number of infected cells present at each frame of each video by using a Laplacian of Gaussian filter to identify GFP+ spots of approximately 8 μ m

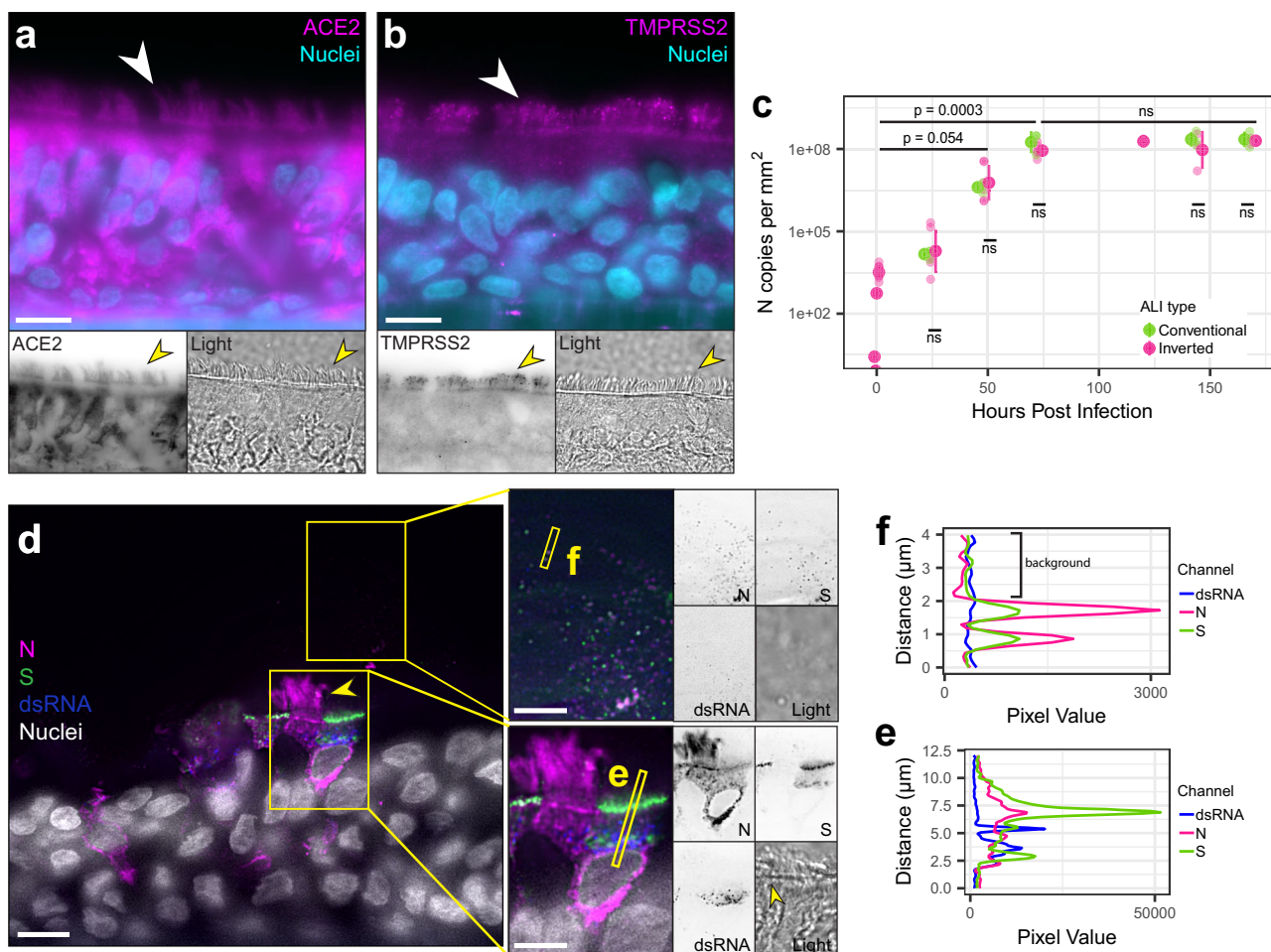


Fig. 2 | Inverted ALI culture model supports SARS-CoV-2 infection. Immunofluorescent images of sections of ALI cultures stained for SARS-CoV-2 entry factors (magenta) and nuclei (Hoescht, cyan). Bottom panels show entry factor staining in inverted grayscale and brightfield. Cilia marked with arrowheads. Scale bar = 20 μ m. Cultures from 2 donors were stained with comparable results. **a** ACE2. **b** TMPRSS2. **c** Copies of nucleoprotein (N) RNA per square millimeter of culture area in mucus collected from inverted (pink) and conventional (green) ALI cultures immediately prior to or at several time points after infection. 1 HPI = post-infection rinse, as an approximation of input virus. Points represent the mean of technical duplicates ($n = 3–6$ ALI cultures across 3 donors per time point per condition). Error bars represent the mean of means \pm standard deviation. Significance by two-sided Welch's *t*-test. **d** Immunofluorescent images of a section of an ALI culture 72 h after SARS-CoV-2 infection stained for SARS-CoV-2 N (magenta), Spike (S, green), double-stranded RNA (dsRNA, blue), and nuclei (Hoescht, white). Results are typical from 3 independent experiments. Thresholding of viral antigens is altered in the right inset panels to highlight dim viral protein puncta among the cilia and mucus. Yellow arrowheads point to cilia. Rightmost panels show single channels in inverted grayscale. Skinny yellow rectangles surround the lines profiled in **e** and **f**. Scale bar = 10 μ m in large image and 5 μ m in insets. **e**, **f** Line profile pixel intensities of cellular (**e**) and mucus (**f**) viral antigen (magenta N, green S) and dsRNA (blue) staining. Source data for all plots are provided as a Source Data file.

around 48–72 HPI, peaking at a median of 114 HPI (Supplementary Fig. 6bc). Infected cells sometimes clearly maintained viability and persisted within the epithelium for multiple days (Fig. 3d, Supplementary Video 10). Nevertheless, overall infection remained relatively low, with peak infection in the most infected culture only ever reaching 3.3×10^4 GFP+ spots or 20% of the total surface area. While the density of GFP+ cells could be much higher in infected foci, large swathes of the surface remained uninfected in most infected cultures.

Infection kinetics in different cultures correlated with the morphology of the infection foci, MCC patterns, and culture artifacts (Fig. 3e, f, Supplementary Fig. 7a, b). Most cultures had comet-like foci, with single infected cells initially appearing around 16–20 HPI and multiple infected cells appearing subsequently downstream of MCC tracks around 36–48 HPI. These cultures generally had larger areas of coordinated MCC, though it could be more disorganized or more rotary. Another subset of cultures had infection appear diffusely over the entire surface of the culture around 36–48 HPI. These cultures reached the highest peak infection and all displayed efficient MCC in a rotary pattern (Fig. 3f). In a minority of cultures, infection was

diameter (Fig. 3b, Supplementary Fig. 5a)³⁸. Spots present at baseline (generally attributable to the background around the rim of the transwell) were subtracted. Because we lack a marker suitable for cell segmentation and 4 \times magnification is often insufficient to segment based on morphology, a spot may be more than one cell (Supplementary Fig. 5a). This occurs often in regions with dense infection or crypts, where cells oriented orthogonal to the imaging plane overlap in Z projections (Supplementary Fig. 5b). The peak number of GFP+ spots and the peak GFP+ fractional area were positively correlated with the number of copies of N RNA in apical rinsate at 120 HPI, validating the metric (Fig. 3c). Isolated GFP+ cells first became apparent around 16–20 HPI, with a median of 10 initial infected cells per culture (Supplementary Fig. 6a). The viral inoculum contained 5×10^5 plaque-forming units (PFU, titered on Vero E6 cells) per well, corresponding to an MOI between 0.5 and 1, so the relative scarcity of early infected cells suggests there are formidable barriers to initial infection in these cultures. After the initial stage of infection, there was considerable heterogeneity in the infection kinetics both within and between donors. For most cultures, the number of GFP+ spots increased rapidly

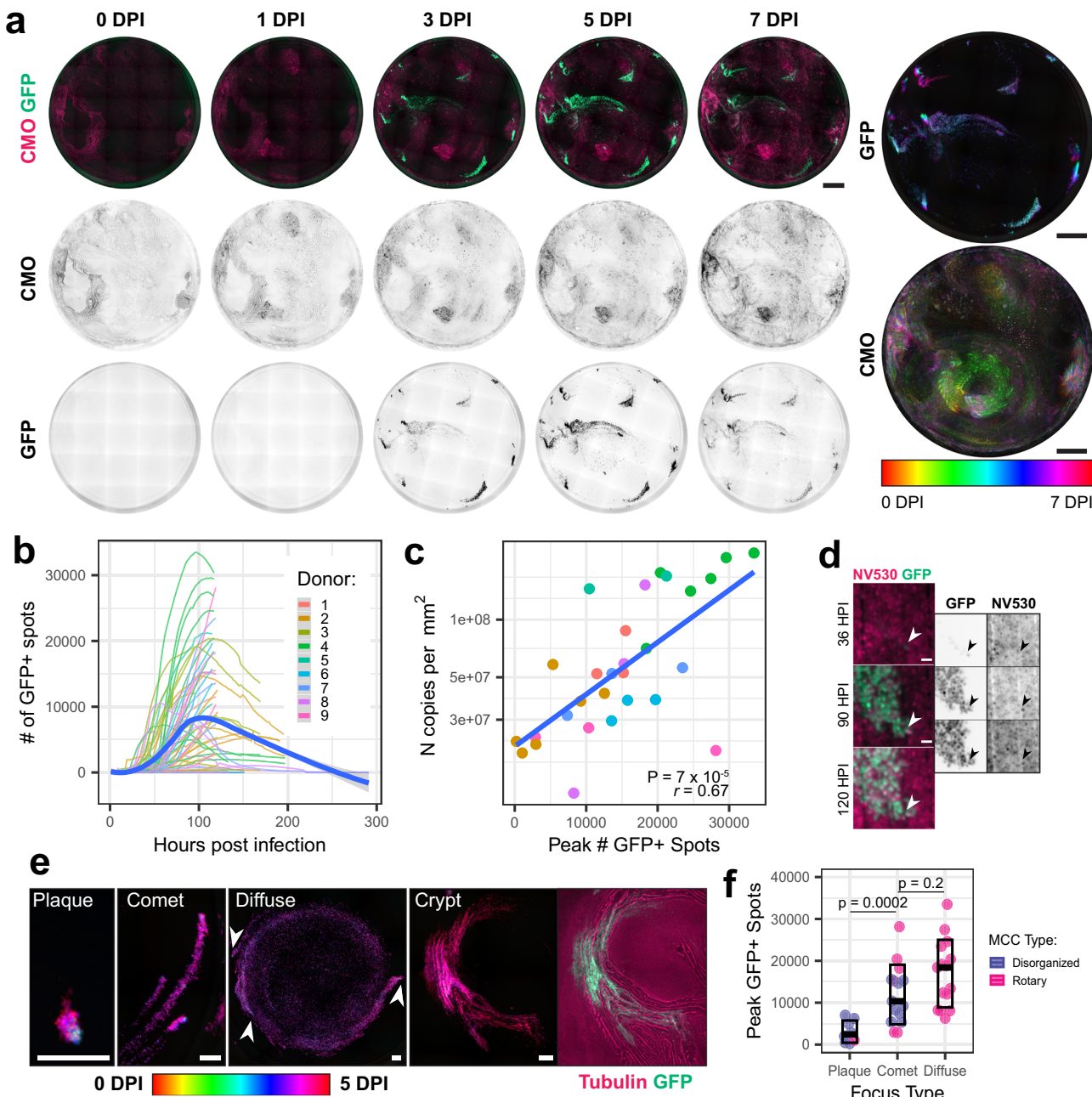


Fig. 3 | Spatiotemporal dynamics of SARS-CoV-2 spread in inverted ALI cultures. ALI cultures from 9 donors were infected with icSARS-CoV-2-eGFP (green) in the presence of the indicated stains and imaged using a 4× air lens every other hour for 5–9 days. **a** Images of one representative culture (from a total of 60 infected cultures) stained with CellMask Orange Plasma Membrane dye (CMO, bright pink) and infected with icSARS-CoV-2/eGFP (spring green) are shown over 7 days of infection. Temporal color code projections of this culture are shown on the right. Scale bar = 1 mm. **b** Graph of GFP+ spots over time in SARS-CoV-2 infected ALI cultures ($n = 3\text{--}11$ cultures for each of 9 donors; 60 cultures total). The bold blue line is a Loess-smoothed trend with standard error in gray. Points are colored by the donor. **c** Scatterplot of peak GFP+ spots versus N RNA concentration per square millimeter of culture area at 5 days post-infection (mean of technical duplicate) from infections of ALI cultures from 8 donors ($n \geq 3$ replicates per donor; 29 cultures total). Pearson's correlation coefficient $r = 0.67$, $p\text{-value} = 7 \times 10^{-5}$.

d Representative time-lapse images of a comet-shaped focus of infection, with SARS-CoV-2-eGFP in spring green & NucView 530 in bright pink. The white arrowhead indicates the first observed infected cell. Scale bar = 10 μm. Result is typical of 5 independent experiments. **e** Representative images of foci of various morphology. Scale bar = 100 μm. The first four images are temporal color code projections from 0 to 5 days post-infection; the image to the far right shows the crypt focus at a single time point with icSARS-CoV-2/eGFP in green and SPY650-tubulin in bright pink. Arrowheads mark comet heads which initiated the diffuse focus. Comparable results were observed in 15/15 independent experiments. **f** Peak GFP+ spots in each culture. $N = 38$ infected cultures from 9 donors, separated by focus morphology type. Points are colored by the MCC pattern of the culture. Black boxplots show the median and interquartile range. $*p = 0.0006$ by two-sided Wilcoxon rank sum test. Source data for all plots are provided as a Source Data file.

restricted to circular plaque-like foci with a high density of infected cells in small, defined areas; these plaques grew slowly and had low peak numbers of infected cells. Most of these cultures had extensive cell migration (4/8) or the hypermobile phenotype (2/8), furrows in the

main culture area (6/8), and disorganized MCC (7/8). A fourth focus type was occasionally observed that appeared restricted to crypts. These foci were identified by the presence of horizontally oriented cells in patterns matching the whorls of the cilia marker. Such foci

developed a high density of infected cells that remained largely confined within the crypt, with apparently limited access to the broader apical surface. Diffuse foci and comets of varying sizes were observed in immunofluorescence of conventional cultures infected with wild-type SARS-CoV-2 WA-1 and in live imaging pilots with an alternate reporter virus (SARS-CoV-2 WA-1/Venus-2A-N) (Supplementary Fig. 8, Supplementary Video 11)³⁹. This suggests that these patterns of infection are not specific to the inverted culture format or the ORF7a-reporter virus.

Linear modeling of N RNA content in mucus showed that in addition to donor-dependent variance, extensive cell migration and foci in crypts were associated with reductions in N concentration while the presence of cyst-type crypts increased N concentration (Supplementary Fig. 7c). These relationships were not significant in modeling of the peak number of GFP+ spots. We suspect that cells within crypts are comparably susceptible to cells within regions of typical morphology, but their limited access to the apical surface both facilitates dense local spread and hinders sampling of shed N RNA. It is also possible that these cells are susceptible to infection but produce less N RNA. Taken together, these data suggest that MCC and ALI culture artifacts including unjamming and crypt formation can impact the spatiotemporal dynamics of SARS-CoV-2 spread.

MCC facilitates SARS-CoV-2 spread

Since MCC patterns in individual cultures correlated with the morphology of SARS-CoV-2 foci and foci directly followed mucus motion, we hypothesized that restriction of MCC would limit SARS-CoV-2 spread independent of the unjamming phenotype. To mechanically restrict MCC, we applied a layer of low melting temperature agarose to the apical surface of the cultures immediately after mucus removal, CMO staining, and infection (Fig. 4a, Supplementary Video 12). As seen in the temporal color code of the CMO channel (Fig. 4b), overlaying the cultures with agarose restricted mucus movement as reflected in the larger areas of static gray (right) as opposed to more saturated colors showing movement over time (left). Imaging of icSARS-CoV-2/eGFP spread following agarose overlay in multiple donors showed a clear restriction of infection to smaller, often plaque-like foci (Fig. 4c, Supplementary Video 12) similar to those observed in individual cultures with disorganized MCC above (Fig. 3e). Quantification of this effect in multiple donors confirmed lower peak infection percentage and slower spread upon agarose overlay (Fig. 4d, e), except for one culture which had infection in an intraepithelial crypt (Fig. 4f, Supplementary Video 13). Cells within crypts are not exposed to the apical surface and thus not accessible to the agarose overlay. Rapid spread within the crypt further suggests that agarose overlay specifically inhibits infection by MCC restriction as opposed to a nonspecific mechanism, such as hypoxia, osmotic changes, or thermal damage to cells during overlay application.

To address this question in a different way, we knocked out axonemal dynein genes in primary HBEs from three donors prior to the differentiation of inverted ALI cultures. Axonemal dyneins drive ciliary motion by generating the sliding motion of microtubule doublets within cilia⁴⁰. *DNAH5* and *DNAI1* were targeted here on the basis of their common occurrence in human primary ciliary dyskinesia and the successful production of *DNAH5* and *DNAI1* KO mice, suggesting that mutations in these genes are well tolerated^{41,42}. After the initial expansion, undifferentiated HBEs were electroporated with in vitro synthesized CRISPR-Cas9 ribonucleoproteins (crRNPs) targeting *DNAH5*, *DNAI1*, *CYPA* as an editing control, or non-targeting guide (NT). Cells then were seeded at high density on the undersides of collagen-coated transwells (Fig. 5a). Multiciliated cells still differentiated and the apical surface of the cultures was tubulin rich as usual (Fig. 5b, Supplementary Fig. 9a).

To determine the impact of these perturbations on ciliary motion, cultures were stained with SPY650-tubulin and visualized by high-

speed video microscopy. For each pixel, the power of the signal at each possible beat frequency (given the sampling rate) was calculated using a Fast Fourier Transform (FFT)-based power spectral density analysis; the frequency that corresponded to the maximal power density for the pixel was taken to be the dominant beat frequency (Fig. 5c)⁴³. The 85th percentile value of power density observed in framewise shuffled videos was used as a threshold for authentic signals. Most such pixels in unshuffled videos corresponded to beating cilia. Compared to the NT & *CYPA* KO cultures, the *DNAH5* and *DNAI1* KO cultures had fewer beating cells (Fig. 5c, Supplementary Video 14). The shape of the ciliary beat frequency distributions in NT and *CYPA* cultures was bimodal, with one population of pixels beating around 10 Hz and another approaching 0 Hz (Fig. 5d). The higher frequency population reflects beating cilia while the lower frequency population appeared to arise from pixels in the path of debris moving through the field of view (FOV). In *DNAH5* and *DNAI1* cultures, beat frequency approached the uniform distribution (Fig. 5d). The fraction of pixels with power density above the 85th percentile of shuffled videos was higher in NT and *CYPA* KO cultures than axonemal dynein KOs (Fig. 5e). As expected given the polyclonal nature of the KO cells, motile cilia were still evident in both axonemal dynein KO cultures, with the *DNAI1* KO cultures having ciliated patches and the *DNAH5* KO cultures having very few motile cilia (Fig. 5c). MCC in each culture was additionally assessed by imaging with NV. In temporal color code projections of NT & *CYPA* KO cultures, we observe central mucus balls and single-color streaks consistent with the rapid motion of apoptotic cell debris during the acquisition of image stacks at each time point, while in *DNAH5* and *DNAI1* cultures we typically observed single-color dots, rainbow traces, or white spots consistent with slower to absent motion of apoptotic cell debris (Fig. 5f).

Each culture was subsequently challenged with SARS-CoV-2/eGFP and imaged over five days. The NT and *CYPA* KO cultures had large diffuse or comet-like foci (Fig. 6a, Supplementary Video 15). In contrast, infection of the *DNAH5* and *DNAI1* KO cultures resulted in smaller comet or plaque-foci, similar to the agarose overlay (Fig. 6a, Supplementary Video 15). Axonemal dynein KO cultures reached lower peak infection & had slower growth in the number of GFP+ cells (Fig. 6b, c). N RNA density in apical rinsate significantly differed between NT and *DNAH5* KO (Fig. 6d), though both axonemal dynein KOs significantly differed in number of GFP+ spots at peak and at days 3 and 4 (Supplementary Fig. 10). Extent of ciliation approximated by fraction SPY650-Tubulin+ area at the initial timepoint correlated only weakly with readouts of infection (Supplementary Fig. 9b, c). Stronger was the correlation of fraction beating area with the peak number of GFP+ spots (Fig. 6e). In sum, these data show that mechanical and genetic perturbation of ciliary motion and MCC inhibit SARS-CoV-2 spread after infection.

SARS-CoV-2 infection modestly inhibits ciliary motion in early infection

MCC facilitates the spread of SARS-CoV-2 early in infection, but this effect is limited. Comet-shaped foci do not grow indefinitely, suggesting that either downstream cells develop resistance to infection or MCC becomes dysfunctional at later time points. In uninfected cultures, mucus movement most often continues for the duration of any given experiment (Fig. 7a). However, in SARS-CoV-2 infected cultures, mucus movement stops at an average of 100 HPI (Fig. 7a). Previous studies have suggested that MCC dysfunction during SARS-CoV-2 infection may be driven by the loss of multiciliated cells, which are the major target of infection in airway epithelium, or by enhanced secretion of MUC5AC-containing mucus by goblet cells as a host defense^{11,17}.

To disentangle the contributions of these factors, we first investigated changes in ciliary motion in infected cells. We acquired ciliary beat frequency movies and 10 \times magnification reference images at multiple FOVs in SPY650-tubulin stained mock and infected cultures,

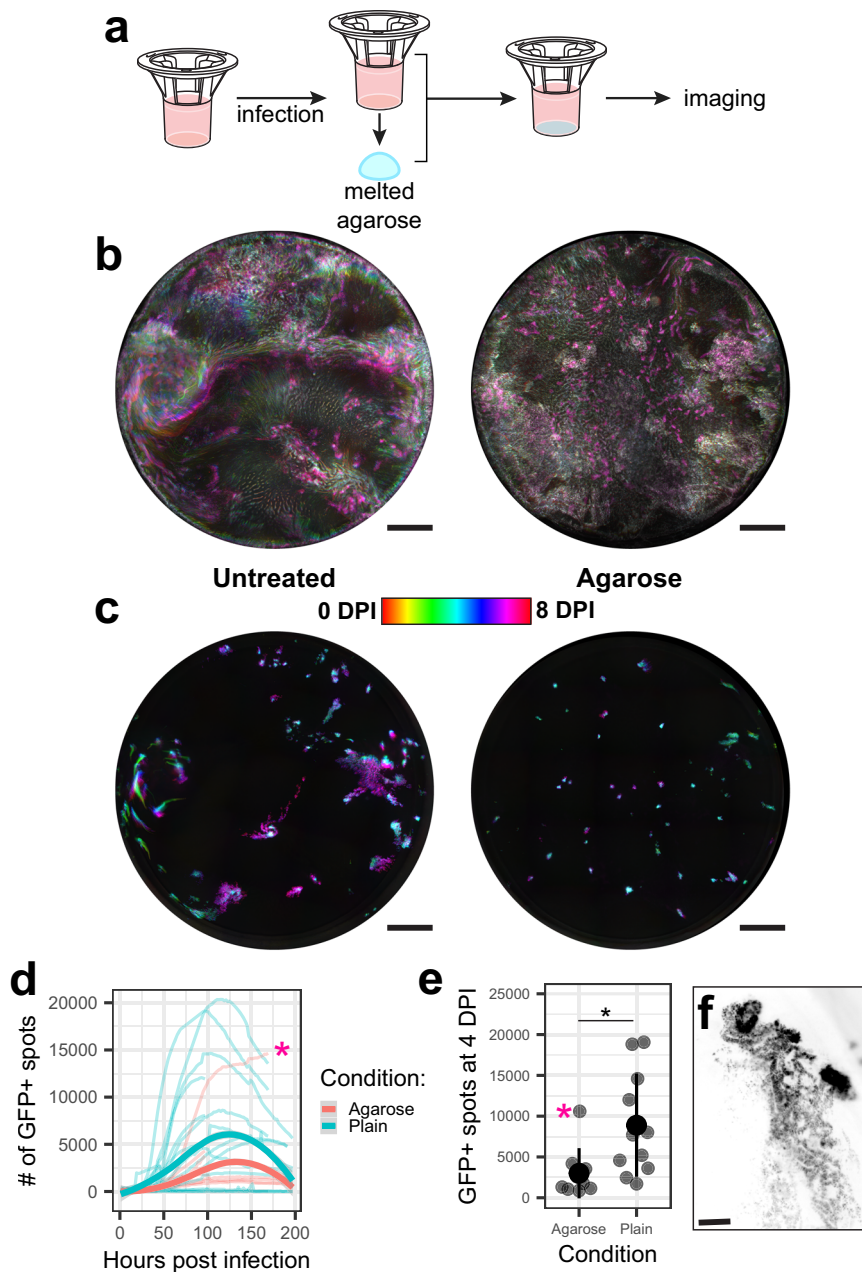


Fig. 4 | Agarose overlay restricts mucus flow and SARS-CoV-2 spread. **a** Schematic of agarose overlay experimental design. **b** Temporal color code projection of CMO signal, and **c** SARS-CoV-2-eGFP signal in representative cultures with (right) and without (left) agarose overlay. Experiments were performed three times with comparable results. Scale bar = 1 mm. Color scale is the same for (**b** and **c**). **d** The number of GFP+ spots in each culture at each timepoint post-infection. Agarose overlay cultures are in red, and no overlay cultures are in blue ($n \geq 3$ ALI cultures per donor per condition for 3 donors). The pink asterisk marks an outlier with infected crypts. Bold lines are Loess-smoothed trends with standard error in

gray. **e** The number of GFP+ spots at 4 days post-infection for each culture shown in (**d**). The pink asterisk marks the same outlier. $*p = 0.007$ by two-sided Wilcoxon rank sum test. Mean \pm standard deviation is shown by the bold points and lines. $N = 10$ ALI cultures from multiple donors per condition. **f** Inverted greyscale image of the GFP channel at 3 days post-infection of an infected crypt in the agarose overlay culture indicated with a pink asterisk in (**d** and **e**). Crypt infection was not typical in these experiments. Scale bar = 100 μ m. Source data for all plots are provided as a Source Data file.

starting from 1 to 5 h post-infection and then daily as possible until 1-week post-infection. Initial FOVs were selected in a spiral pattern over the culture surface; once the GFP signal became visible, additional FOVs were added centered on GFP+ cells in infected cultures and randomly in mock-infected cultures. Between beat frequency measurements, we acquired 4 \times magnification whole culture time lapses as usual. We cross-correlated the reference images and whole culture time lapses to identify trackable single cells, following them from the time the GFP signal became visible to the loss of the GFP signal (Fig. 7b,

Supplementary Vid. 16). Loss of the GFP signal was presumed to result from either cell death or detachment from the monolayer and thus likely imminent cell death. Infected cells remained GFP+ for between 26 and 97 h, with a median GFP+ lifetime of two days (Fig. 7c). Survival times were reduced for Orf7a + WAI/N-2A-Venus, though the median lifetime was comparable (Supplementary Fig. 11, log-rank $p = 0.043$). The multi-day GFP+ survival times we observe are thus not an artifact specific to the ORF7a-reporter virus, though they may be some hours longer than a non-reporter virus. The true duration of infection is

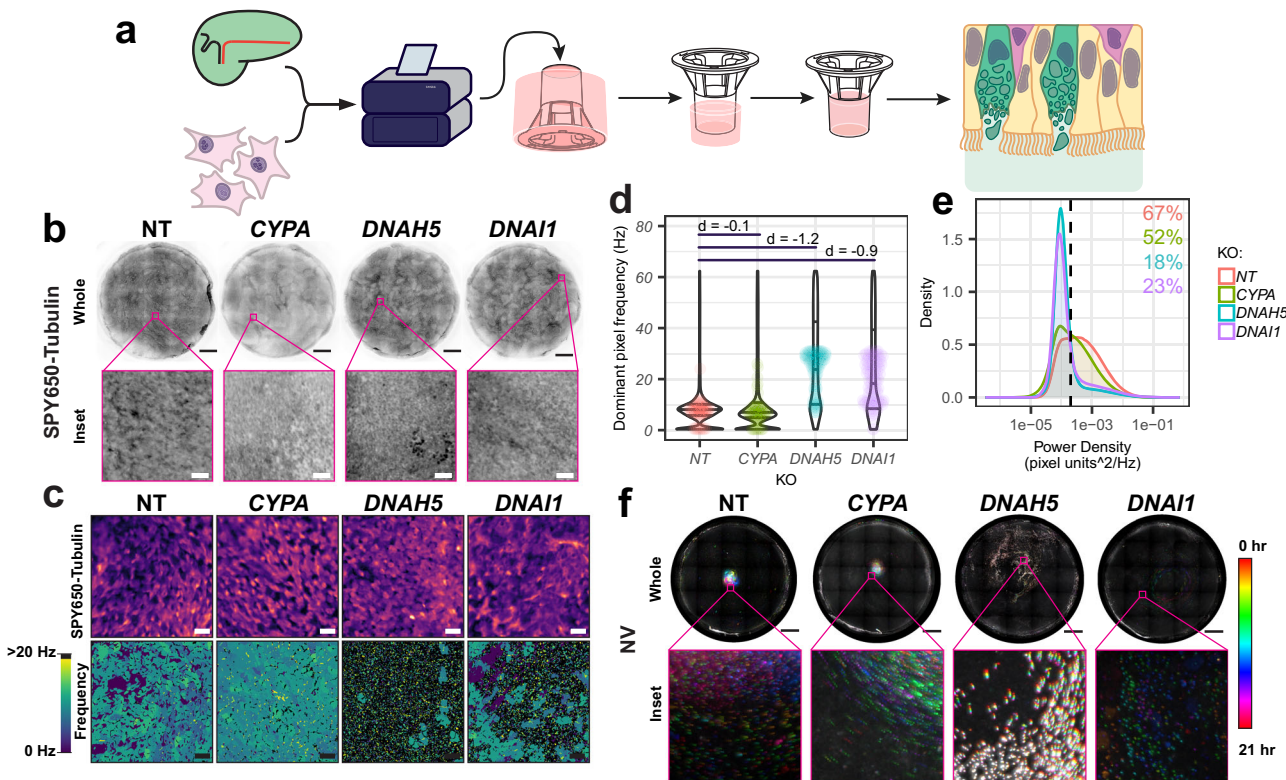


Fig. 5 | Genetic perturbation of ciliary motion. **a** Schematic for the production of gene knockout in inverted ALI cultures. **b** Images of SPY650-tubulin signal (inverted greyscale) from representative KO cultures. Top panels are whole cultures (scale bar = 1 mm). Bottom panels are insets marked with pink in the whole culture images (scale bar = 50 μm). **c** Single frames of representative denoised SPY650-tubulin videos in knockout ALI cultures (top, magma colormap). The dominant beat frequency in Hz of each pixel of the same movies (bottom) with beating multiciliated cells visible as midtone gray patches. Scale bar = 20 μm. **b, c** Representative images are derived from the same 4 cultures. Results were typical across 2 experiments. **d** Plots of the distribution of beat in SPY650-tubulin movies of knockout ALI cultures ($n = 5\text{--}6$ cultures per KO, 3 donors). Bee swarms of median beat frequency in

each FOV are overlaid on violin plots of pixel beat frequency. 0.3–0.6 mm² per culture (~1–2% of total culture area) was surveyed per culture. Cohen's d effect sizes on aggregate pixel distribution reported. **e** The distribution of power density in pixels from NT and each knockout. Dashed line is the 85th percentile of power density in frame-shuffled videos, and numbers in the top-right are the percentile of pixels falling above this threshold for NT and each knockout. **d, e** Points and lines are colored consistently by KO. **f** Temporal color code projections of 20-h time lapses of NucView 530 signal from representative ALI cultures during infection. Top panels are whole cultures (scale bar = 1 mm). Bottom panels are insets marked with pink (scale bar = 50 μm). Source data for all plots are provided as a Source Data file.

longer owing to the lag time between infection and detectable GFP production, which is on average 16 h for the first generation of infected cells.

We observed a variety of cell fates (Fig. 7d). Some cells were never observed beating and persisted for a day or less; others were observed beating and persisted only briefly or for extended periods of time. Still others began non-beating but were later observed beating. The largest population appeared to be persistently beating cells (Fig. 7b, d). Of cells that were tracked from 24 or 48 h post-infection, 19/23 beat with normal beat frequency at the last beat frequency measurement prior to death (Fig. 7b, d). Tracked cells had on average 2.5 daily ciliary beat frequency measurements with values compatible with ciliary motion during their GFP+ lifetime, with 11/23 cells being observed beating for 3 or 4 days (Fig. 7d). A cell that is beating and ensconced within the monolayer must be alive and performing metabolic activities to support the ciliary motion, so these findings suggest that multiciliated cells may retain viability and function for days following SARS-CoV-2 infection with a rapid decline in function in the hours preceding death or loss of contact with neighboring cells. Furthermore, 8/11 of the long-surviving cells initiated foci or appeared to infect neighboring cells, indicating that cells with the long-surviving phenotype can be productively infected.

Tracking individual infected cells over time relies on FOVs with atypically sparse infection patterns and is complicated by the formation of syncytia. To better survey the population beat frequency of the infected & bystander cells over time, we performed per-pixel

quantification of the above infections again using an FFT-based power spectrum analysis. The fraction of pixels with frequency between 2 and 15 was used to approximate the culture area covered with beating cilia (Fig. 8a, Supplementary Fig. 12). Fraction beating area increased over time in both mock and infected cultures, likely as a result of improved signal detection as the SPY650-tubulin incubation period increased. Though comparable or higher up to 72 h post-infection, afterward the beating fraction of infected cultures decreased significantly (Bonferroni adjusted Wilcoxon $p = 1 \times 10^{-6}$ at 96 HPI). There was heterogeneity between fields of view, with the variance of beating fraction in FOVs from infected cultures increasing over time. Despite the decrease in beating cilia coverage, many FOVs in infected cultures were dense with beating cilia even at one-week post-infection. Beat frequency within the 2–15 Hz range was comparable until 168 HPI, when the infected cultures showed a lower median beat frequency and a broader distribution (Fig. 8b, Supplementary Fig. 12b). At earlier time points slight differences could be seen, with infected cultures becoming enriched in a slightly faster-beating population. Pixels increasingly began to shift to a low-power population starting at 96 h post-infection (Supplementary Fig. 12c). This may reflect decreasing regularity of the beat, which dilutes signal power across multiple frequencies, or decreasing cilia density, which reduces the power of a regular SPY650-tubulin signal. These data suggest that infected ALI cultures suffer decreases in motile area by 96 h post-infection, likely due to loss of infected multiciliated cells. These decreases are not numerically large but may be

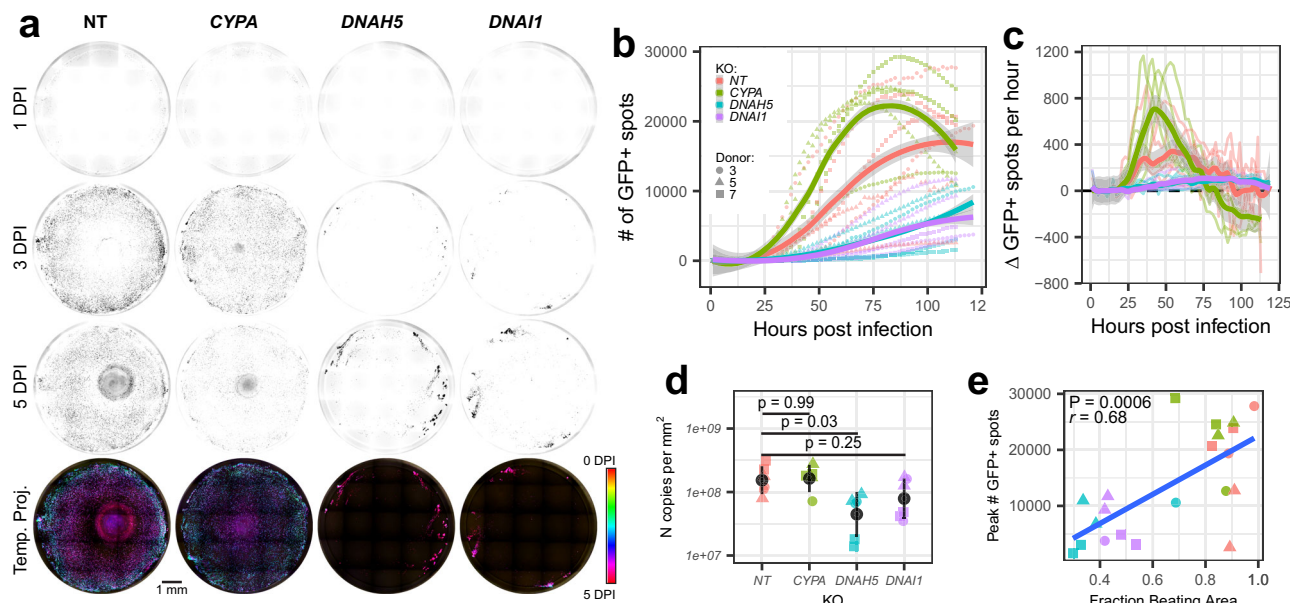


Fig. 6 | Ciliary motion KO inhibits SARS-CoV-2 spread. **a** Snapshots of GFP signal (inverted grayscale) following SARS-CoV-2/eGFP infection of representative knockout cultures at the indicated time points. The bottom panels are temporal color code projections of the entire time course. Scale bar = 1 mm. Representative images are derived from the same 4 cultures. Results were typical across 2 experiments. **b** Number of GFP+ spots at each timepoint for each culture ($n=5\text{--}6$ cultures per KO, 3 donors). Bold lines are Loess-smoothed trends with standard error in gray. **c** First derivative of splines fitted to GFP+ spots count at each frame of videos summarized in (b). Spar = 0.1 for spline fitting. Lines are colored by KO. Bold

lines are Loess-smoothed trends with standard error in gray; span = 0.1. **d** Copies of nucleoprotein RNA per mm² of culture area in mucus collected from all knockout ALI cultures at 5 days post-infection. $N=5\text{--}6$ cultures from 3 donors (shapes) for each condition. Significance calculated by one-way ANOVA followed by post-hoc analysis using Tukey's HSD (two-sided) where significant. Black dot and bars show mean \pm standard error. **e** Scatterplot of peak GFP+ spots versus fraction beating area (power density $>2\text{e-}4$) for all KO cultures. Pearson's correlation coefficient $r=0.68$, $p\text{-value}=0.0006$. **b**, **c**, **d**, **e** Points and lines are colored consistently by KO. Source data for all plots are provided as a Source Data file.

functionally significant. Subtle changes in ciliary motion may occur earlier, even before many cells become infected.

To understand whether these differences between mock and infected cultures are driven by infected cells or bystander cells, we compared fraction beating area and beat frequency between neighboring GFP+ and GFP- pixels in the same FOV (infected & near GFP-), GFP- pixels in FOVs that contained no GFP+ pixels in infected cultures (far GFP-), and all pixels from mock cultures (Fig. 8c, d, Supplementary Fig. 13). Beating area of all four categories was similar until 72 HPI (Fig. 8c). From 72 to 168 HPI the beating fraction of GFP+ pixels differed from that of far GFP- pixels, suggesting a loss of ciliary motion among infected cells at these times. The beat frequency distribution of GFP+ pixels was broader and/or lower than that of mock pixels at all time points, suggesting that infection alters ciliary motion prior to loss of motion (Fig. 8d, Supplementary Fig. 13b). That the distribution approached but did not reach the uniform distribution, and that the mean fraction beating surface area was above the threshold expected by chance (0.23, the fraction of potential frequency values spanned by the 2–15 Hz range) is consistent with our cell tracking data suggesting that some but not all infected cells retain ciliary motion for extended periods of time.

At 168 HPI the far GFP- pixels began to differ from mock cultures, with significantly lower beating fraction, suggesting indirect effects of viral infection impact ciliary motion. Prior to that time, the far GFP-CBF distributions were enriched in the higher-frequency population. The near GFP- distributions started enriched in this population, but ended with lower median beat frequency and a tighter distribution than the GFP+ pixels, suggesting that cells near infected cells beat more slowly late in infection. There are likely multiple factors contributing to these complex bystander effects. The 16 h lag time between infection and detectable GFP production means that some fraction of neighboring GFP- pixels likely correspond to newly infected cells. Local differences in mucus rheology impact ciliary motion, as cilia tips contact and exert force on the mucus layer during their

effective stroke, so a stiffer mucus layer reduces ciliary beat frequency. Excessive mucus is also optically unfavorable for detecting ciliary motion, which both broadens beat frequency distribution and reduces fraction beating surface area.

To understand how mucus secretion impacts MCC in infection, we first measured changes in MUC5AC secretion. Dot blotting of apical rinsates showed that MUC5AC content increased over time, consistent with other observations (Fig. 9a, b)¹⁷. To test whether the mucus influenced the spatial restriction of infection at later timepoints, we rinsed cultures at 120 HPI, at or shortly after the peak of infection. Cultures that displayed rotary MCC early in infection resumed rotary MCC, with apoptotic cells moving in mucus over foci of infection (Fig. 9c). Those with comet-like foci saw the extension of the comets (Fig. 9d, Supplementary Video 17). In most cultures rinsing initially decreased the number of GFP+ spots, likely due to the removal of loosely affiliated moribund GFP+ cells, but later the number of GFP+ spots increased from the post-rinse nadir (Fig. 9e, f). In cultures where no decrease or minimal decreases were observed, the slope of the increase increased post-rinse (Fig. 9f). This suggests that stalled infection and cessation of MCC in infected ALI cultures is primarily due to secretion of soluble factors, likely including mucus, and not solely depletion of infected multiciliated cells.

In vivo, mucus is propelled continually toward the pharynx and swallowed. In ALI cultures, the mucus accumulates until rinsed. To better understand how MCC shapes infection when supraphysiologic mucus accumulation is limited, we rinsed cultures daily for the first four days of infection, then at 7 days post-infection (Supplementary Fig. 14a, Supplementary Video 18). Decreases in GFP+ spots post-rinse were observed from 60 HPI on, increasing in magnitude over time (Supplementary Fig. 14b, c). Increases post-rinse (either absolute or from a post-rinse nadir) were seen in 6/6 cultures to 2 days post-infection; in 5/6 at 3 days post-infection; in 3/6 at 4 days post-infection; and in 0/6 at 7 days post-infection. After the 4-day post-infection rinse,

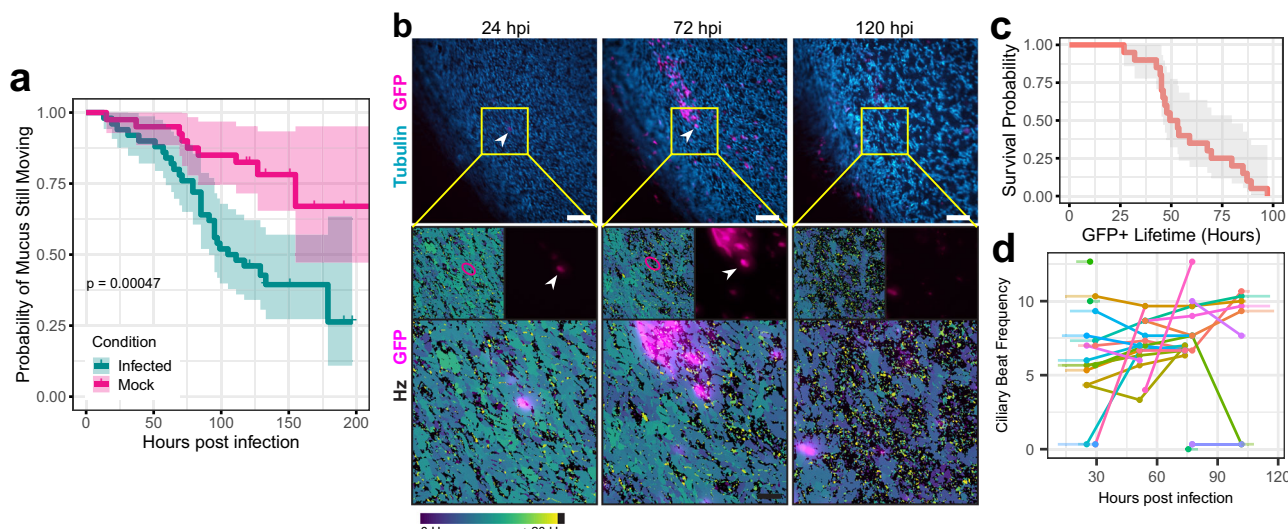


Fig. 7 | Effects of SARS-CoV-2 infection on ciliary motion. a Survival curves showing time to cessation of mucus motion in infected (blue) or mock (pink) cultures ($n = 9$ donors, \geq three ALI cultures per donor). $p = 5 \times 10^{-4}$ by log-rank. The translucent areas show 90% confidence intervals. **b** Live imaging snapshots of an infected cell identified at 24 hpi & followed to 72 hpi. Tubulin and SARS-CoV-2/eGFP are visualized in blue and bright pink, respectively (top). Scale bar = 200 μ m. Beat frequency in Hz of the central (FOV) is shown below in greyscale with infected cells overlaid in magenta (bottom). Scale bar = 50 μ m. Arrowheads (top) or pink circles

(bottom) identify the initial infected cell. **c** Survival curve of GFP+ lifetime of tracked infected cells in ALI cultures. $n = 28$ cells from 4 cultures of 3 donors. Red line is the fraction of tracked cells remaining GFP+ and in the epithelium over time. Gray area is 90% confidence interval. **d** Plot of ciliary beat frequency over the lifetimes of tracked cells in (c). Lines and points of a single color reflect a single cell. Bold points and lines mark and span ciliary beat frequency measurements. Transparent lines extend to the time of initial cell detection and time of loss of GFP signal in whole culture time lapses when such time was captured.

among the 3 cultures where an outright increase in GFP+ spots was not observed, a decrease in the rate of decline was observed (Supplementary Fig. 13b, c). Since the number of GFP+ spots at a given time is a function of the numbers of dying and newly infected cells, these post-rinse decreases in rate of decline likely also reflect newly infected cells (rinsing being unlikely to extend the life of long-infected cells). This is consistent with an inhibitory role of mucus even when accumulation is limited.

Discussion

Here we demonstrate methods to perform live imaging of SARS-CoV-2 infected ALI cultures, revealing some of the complexities of how MCC impacts viral distribution and infection. At first an efficient barrier to infection, after initial penetration MCC facilitates rapid infection kinetics by spreading virions caught in mucus. Later in infection, altered mucus secretion inhibits MCC and restricts the growth of foci of infection.

Though MCC-mediated spread seems plausible for any respiratory virus with apical entry and shedding, viruses may differ in the extent to which they develop the characteristic cometlike foci in ALI culture. Measles virus develops dense plaques, the en bloc shedding of which may be key to measles' exceptional transmissibility^{44,45}. RSV and human parainfluenza virus may display comet-shaped foci early in infection, but for these viruses, the foci merge and grow to occupy the majority of the culture surface area, rather than remaining distinct as is often the case in SARS-CoV-2 in the current study^{5,46}. For the influenza A virus, no published images of cometlike foci were identified^{47,48}. Comparisons between viruses based on published literature are challenging owing to differences in infection, culture conditions, and imaging protocols. For example, even in SARS-CoV-2 published en face images are often plaque-like^{22,49}. With that caveat, differential interaction with components of MCC may represent an underappreciated facet of host-pathogen interaction. Viruses may modulate their focus phenotype & spread kinetics by altering their cytotoxicity, interactions with mucus, or cytokine secretion. For example, influenza viruses modulate their interactions with mucus & the glycocalyx with their

surface hemagglutinin and neuraminidase activities^{50–52}. The balance between the two activities affects mucus penetrance and could lead to different focus morphologies between strains with different activity levels. Later in infection, it is well established that SARS-CoV-2 impairs MCC^{11,17}. Reports on human disease find increased mucus secretion and damaged ciliated epithelium⁵³. In ALI cultures increased MUC5AC secretion has been observed, and the finding that SARS-CoV-2 preferentially infects multiciliated cells has led some to conclude that multiciliated cell depletion is a major cause of MCC dysfunction in SARS-CoV-2 infection^{11,17}. Our work complements these studies by showing that while there is an increase in dysfunctional ciliated cells, the impact of that dysfunction is relatively minor owing to the limited density of foci of infection, and mucus secretion is likely the major factor limiting MCC in the first week of infection. The finding that infected cell fates are highly variable is intriguing, particularly in light of studies on IAV which suggest that minorities of infected cells drive the antiviral response as a consequence of both preinfection cell state and viral factors^{54,55}. Because we used a reporter virus with a considerable lag time between infection and detectability and only sampled beat frequency daily, we likely biased our single-cell dataset toward long-surviving cells. However, we did observe a range of cell fates including some short-lived infected cells.

Live imaging is a particularly useful tool for ALI culture studies of host-pathogen interactions. ALI cultures are the gold standard for cell culture-based studies of the human airway, expressing similar profiles of surface proteins & proteases to the native epithelium, but vast within-donor heterogeneity and the challenges of scaling up ALI culture can make answering questions about dynamic & variable host-pathogen interactions unfeasible. The set of tools we have developed allows us to characterize in detail and follow the course of infection spatially within individual cultures, permitting inferences that would be challenging to make based on fixed samples. The combination of SPY650-tubulin and NV is particularly useful since it allows observation without perturbing the apical surface, and because apoptotic cells ejected from the epithelium are a native substrate of MCC. The use of air lenses with a high depth of field also facilitates long-term imaging

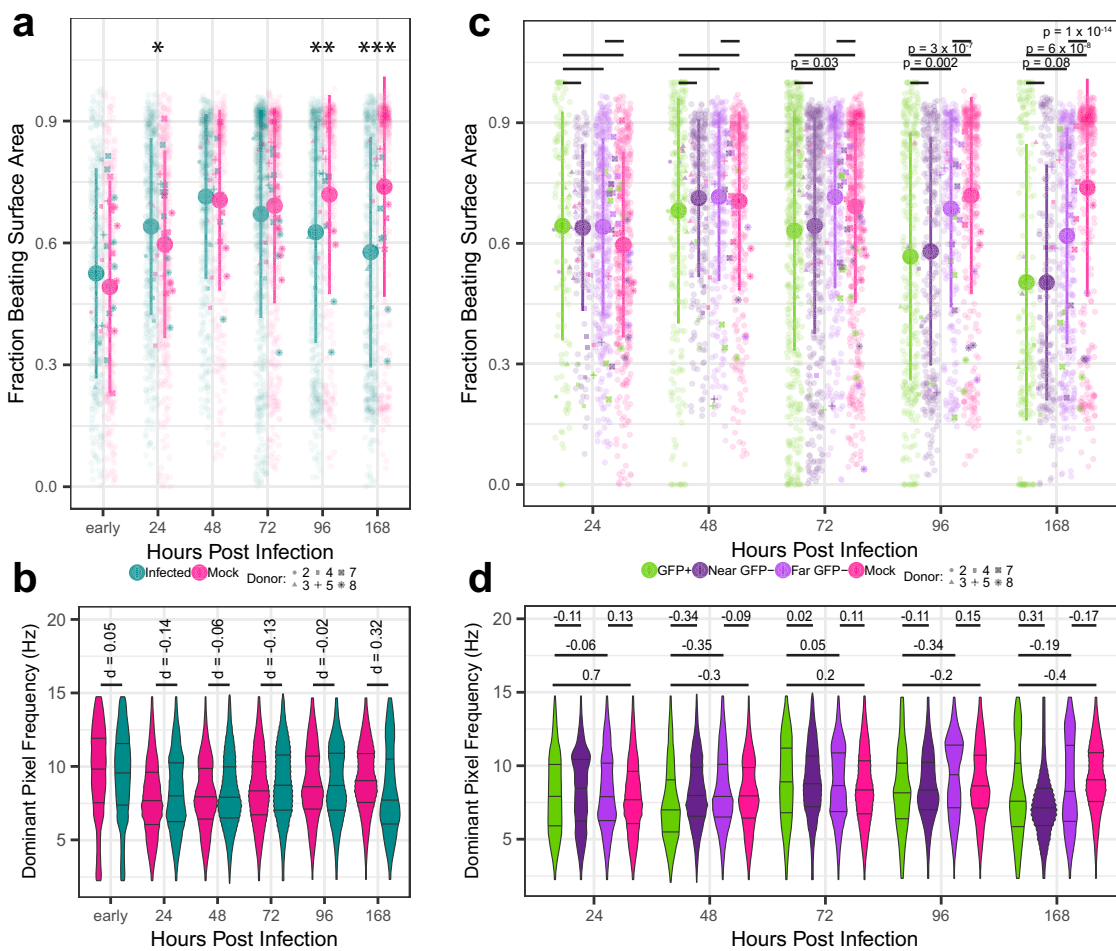


Fig. 8 | Effects of SARS-CoV-2 infection on ciliary motion on a whole-culture scale. **a** The fraction of pixels plausibly reflecting ciliary motion (frequency between 15 and 2 Hz) in each FOV for mock-infected (pink) and SARS-CoV-2 infected (blue) cultures over time. 5 independent experiments were conducted with variable timing scheme and culture allocation; 58 cultures from 6 donors were used in total with an average of 30 FOVs per culture per timepoint. Each FOV is 0.0274 mm². Translucent dots are FOVs; mean and standard deviation are shown opaque; opaque signs are per culture means. Significance by two-sided Wilcoxon rank sum test with Bonferroni post hoc correction. **p* = 0.003. ***p* = 1.7 × 10⁻⁷. ****p* < 2 × 10⁻¹⁶. **b** Violin plots of beat frequency of each beating pixel for all FOV shown in (a). Vertical lines within each violin mark the median and interquartile range. Cohen's *d* is shown for infected-mock comparisons at each time point. **c** The fraction of beating pixels in subsets of FOVs from mock and infected cultures

(shown in aggregate in a) stratified and colored by proximity to GFP signal. Near GFP- pixels are from FOVs that contain GFP+ pixels and far GFP- pixels are from FOVs in infected cultures that do not contain any GFP+ pixels. 5 independent experiments were conducted with variable timing scheme and culture allocation; 58 cultures from 6 donors were used in total with an average of 30 FOVs per culture per timepoint. Each FOV is 0.0274 mm². Translucent dots are FOVs; mean and standard deviation of FOV values are shown opaque; opaque signs are per culture means. Significance by two-sided Wilcoxon rank sum with Bonferroni post hoc correction. **d** Violin plots of beat frequency of beating pixels in mock and infected cultures, with those from infected cultures stratified and colored by proximity to GFP+ pixels. Vertical lines within each violin mark the median and interquartile range. Cohen's *d* is shown for infected-mock comparisons at each time point. Source data are available on Dryad, <https://doi.org/10.5061/dryad.7wm37pw0r>.

by preserving the air-liquid interface. No specialized or excessively costly tools are required, so this method should be readily transferable to other groups. In this work, we largely relied on 4x magnification scans in order to understand phenomena across the entire culture surface, but time-lapse imaging with 10x air lenses is possible and provides more detailed views of individual infected cells. This could enable a single-cell phenomics approach in live ALI cultures, particularly if a suitable junctional marker is identified.

Cell culture models may differ from the tissues they resemble in subtle but significant ways. In humans, mucus is unidirectionally transported out of the airway and does not accumulate and recirculate over the epithelium. We show that mucus contents impact the course of infection and that disrupting mucus contents can have varying effects. This suggests that ALI cultures may poorly model infection dynamics in some aspects, as mucus laden with virions, debris, cytokines, interferons, and more repeatedly passes over the same patch of cells, potentially affecting the spatiotemporal structure of infection.

Additionally, cell migration likely constituting epithelial unjamming affects many inverted ALI cultures in this study. Heavily afflicted cultures differ from healthy ones in surface topology and MCC, and when infected are more likely to have plaque-like foci. Infection in these cultures might reflect the spread of infection in disease states such as asthma rather than the healthy airway. Though the inverted cultures used in this study are seldom used by others, we have observed conventional ALI cultures with extensive furrowing and spiral-like morphology characteristic of the unjamming phenotype during other projects, suggesting that it is not unique to this model. Appreciation of unjamming transition as a phenomenon seems to be rare among virologists working with ALI cultures, perhaps owing to the difficulty of noticing cell migration in a system seldom imaged live.

Other limitations of live imaging of viral infection include the inherent tradeoffs of a reporter virus. We rely on a reporter virus lacking ORF7a¹. SARS-CoV-2 ORF7a is known to have various roles in infected cells including BST2 and MHC class I antagonism^{26,56}. While its

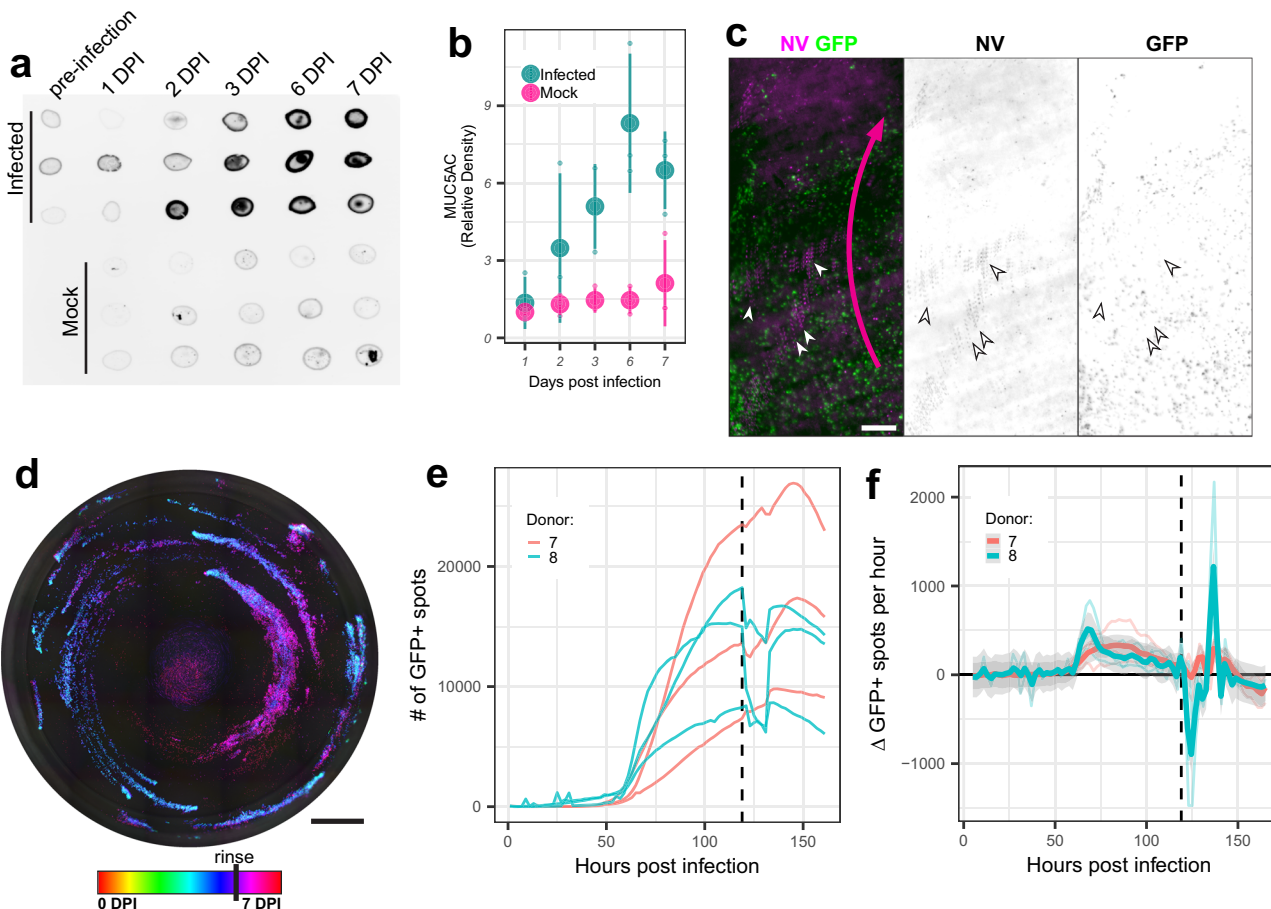


Fig. 9 | Effects of SARS-CoV-2 infection on mucociliary clearance. **a** MUC5AC dot blot on apical rinsates from infected and uninfected cultures over time. DPI = days post-infection. N=1 culture from each of 3 donors per time per condition. **b** Quantification of MUC5AC signal in a. Infected cultures in blue and mock in pink. Error bars are mean \pm standard deviation. N=1 culture from each of 3 donors per time per condition. **c** Projected image showing apoptotic nuclei tracks (NucView 530, magenta) moving over a focus of infection (GFP, green) over the course of 0.8 s shortly after mucus rinses at 120 hpi. Right panels are inverted greyscale single channels. Field of view is at the edge of a larger circular focus underlying a mucus disc. Arrowheads point to moving NV puncta; curved pink arrow shows the direction of rotation of the larger mucus disc. Scale bar = 200 μ m. Representative image from one experiment with 3 replicates for each of two donors. **d** Temporal color code projection of the GFP channel of a whole infected culture with a mucus rinse at 120 hpi (one representative image). Scale bar = 1 mm. Representative image from one experiment with 3 replicates for each of two donors. **e** GFP+ spots at each timepoint for 120 hpi rinsed cultures (n = 3 replicates for two donors). The vertical dashed line marks the time of rinse. Lines are individual cultures colored by the donor. **f** First derivative of splines fitted to GFP+ spots count at each frame of videos summarized in (e). Spar = 0.1 for spline fitting. Lines are colored by the donor. Loess fit line with span = 0.05 shown in bold; the gray outline is the standard error. Source data for the blot and all plots are provided as a Source Data file.

image from one experiment with 3 replicates for each of two donors. **d** Temporal color code projection of the GFP channel of a whole infected culture with a mucus rinse at 120 hpi (one representative image). Scale bar = 1 mm. Representative image from one experiment with 3 replicates for each of two donors. **e** GFP+ spots at each timepoint for 120 hpi rinsed cultures (n = 3 replicates for two donors). The vertical dashed line marks the time of rinse. Lines are individual cultures colored by the donor. **f** First derivative of splines fitted to GFP+ spots count at each frame of videos summarized in (e). Spar = 0.1 for spline fitting. Lines are colored by the donor. Loess fit line with span = 0.05 shown in bold; the gray outline is the standard error. Source data for the blot and all plots are provided as a Source Data file.

effects on apoptosis in infection have not been characterized, over-expression studies suggest ORF7a is a pro-apoptotic factor and its homolog SARS-CoV-1 ORF7a is known to induce apoptosis^{57–60}. We find that infected cells can retain viability and ciliary function for days after infection. This could be a mechanism by which the virus facilitates its spread- an infected cell that can remain functional as it produces virions may spread infection farther than a cell that dies quickly. While we observed similar foci of infection with wild-type WA-1 and a reporter virus with intact ORF7a, the survival time of infected cells with the alternate reporter was somewhat reduced. Median survival time remained comparable at approximately 2 days, but we did not observe the extended survival times out to 4 days seen with our primary reporter virus. This suggests that the lack of ORF7a may improve cell survival post-infection, but that multi-day survival times are still seen. Circulating SARS-CoV-2 strains also contain ORF7 mutations, which could affect its function during infection^{61–63}. It is also possible that the lag time of both reporter viruses causes us to miss many short-lived infected cells.

People with conditions that impair MCC are more vulnerable to respiratory infections. However, this vulnerability is largely to bacterial

pathogens, and when an increased risk of adverse COVID-19 outcomes is observed, it is typically in subpopulations with advanced lower lung disease secondary to bacterial colonization^{64,65}. In this study, MCC impairment inhibits viral replication. Since viral infection likely spreads to the lower lung by inhalation of aerosols generated during speech and singing, it is possible that the smaller plaques and lower viral load we see are still sufficient to seed the lower lung, where pathology occurs¹. Epithelial repair outcomes may also differ when MCC is impaired. Though we did not examine post-infection repair in this study, shedding of isolated cells in diffuse foci may be a less traumatic injury to the epithelium as shedding occurs to some extent in health, while loss of clumps of cells in plaque-like foci likely requires more mobilization of the epithelium^{66–69}. Further work is necessary to characterize epithelial repair mechanisms and outcomes after different densities of infection.

Methods

Research safety approval

All experiments involving replication-competent SARS-CoV-2 were performed in Biosafety Level 3 (BSL3) containment facilities following

approved standard operating procedures approved by the Institutional Biosafety Committees of Northwestern University or the Sanford Burnham Prebys Medical Discovery Institute.

ALI culture

Commercially available primary bronchial epithelial cells (Lonza CC-2540) were initially expanded to 20–50 million cells in PneumaCult Ex Plus medium (Stemcell #05040) on collagen-coated flasks, then cryopreserved in aliquots of 7.5×10^5 cells. To produce inverted ALI cultures, aliquots from this initial passage were further expanded in collagen-coated 75 cm² flasks, then trypsinized and seeded on the underside of 0.4 µm pore polyester cell culture supports (Corning #3470 or Celltreat #230635). Prior to seeding, the undersides of the inserts were coated with 0.1 mg/mL type I collagen (Advanced Biomatrix #5005) diluted in distilled water, equilibrated to 37 °C, and then placed upside down in 12 well plates flooded with warm Ex Plus medium sufficient to maintain moisture on the polyester membrane. 10⁵ cells in 100 µL media were gently pipetted onto the exposed underside of the membrane and returned to the incubator. The 12 well plates were fitted with 3D-printed adapters to raise the lids to avoid contact with the cell suspension. After overnight attachment, cell culture supports were inverted and placed in 24 well plates with Ex Plus medium in the basal and apical compartments. Upon confluence, cultures were fed with PneumaCult ALI medium (Stemcell #05001) in the cup of the cell culture support (Fig. 1a) and an air-liquid interface was established by removing media from the 24-well plate. ALI medium was changed daily for the first few days, then every 48–72 h thereafter. Inverted ALI cultures were kept in 24 well plates with slightly taller wells than standard (Falcon 353047) to prevent mucus bridging. The mucus was removed by apical PBS (Corning 21-040-CV) rinse weekly from the 3rd week or the beginning of mucus secretion. To rinse, cultures were incubated with 600 µL PBS at 37 °C and 5% CO₂ for 30–45 min, then the loosened mucus and excess PBS were aspirated. Cultures were considered differentiated when mucus secretion and ciliary motion were evident, from 4 to 6 weeks. Experiments were performed with 6–12 week old cultures. During infections, media changes were performed as usual, but mucus rinses were deferred for infections lasting longer than one week unless specifically stated otherwise.

Conventional ALI cultures were produced by identical procedures, save flipping the transwell supports.

Cells & viruses. Vero E6 and Vero CCL81 cells were maintained at 37 °C and 5% CO₂ in DMEM (Corning) supplemented with 10% fetal bovine serum (Atlanta Biologics), 1x PSG (Gibco), 10 µM HEPES (Gibco), 1 µM sodium pyruvate (Gibco), and 1× MEM NEAA (Sigma). SARS-CoV-2 USA/WA1-2020 (BEI NR-52281) and ic-SARS-CoV-2-eGFP (BEI NR-54002) were propagated in Vero CCL-81 cells (ATCC CCL-81). Virus stocks were thawed, then diluted in PBS with 3% BSA, 1.1 mM CaCl₂, and 2.2 mM MgCl₂. 90% confluent flasks were incubated with 0.01 MOI virus for 1 h at room temperature, rocking every 15 min. Serum-free media (as described above sans fetal bovine serum) was added to the flask. Cells were incubated at 5% CO₂ and 37 °C for 48 h, then the supernatant was harvested, centrifuged at 4000 × g for 10 min to reduce cell debris, aliquoted, and stored at -80 °C. An uninfected flask was processed in parallel to produce an equivalent supernatant for mock infections. The virus was titrated by plaque assay.

Viral quantification by plaque assay. Viral stocks were serially diluted in DMEM, then incubated on confluent Vero E6 cells at warm room temperature (28 °C) for 1 h, rocking every 15 min. The inoculum was then removed, the monolayer rinsed twice with PBS, and the cells covered with 1.2% microcrystalline cellulose (Sigma 435244) MEM. 72 h after infection, the cellulose overlay was carefully removed and the monolayers fixed and stained with 4% formaldehyde, 20% ethanol, and 0.2% crystal violet. Plaques were manually counted.

Viral quantification by qPCR. Apical rinsates from infected ALI cultures were inactivated by heating to 60 °C for 30 min or 80 °C for 10 min as required by BSL3 Standard Operating Procedures (SOPs). RNA was extracted using a QIAamp Viral RNA Mini Kit (cat #52906) per the manufacturer's directions. Viral load determination was performed by quantitative reverse transcription and polymerase chain reaction (qRT-PCR), using the CDC 2019-nCoV RT-PCR Diagnostic Panel with N1 and RNase P probes from IDT (N1 probe: #10006832, N1 primers: #10006831 and #10006830, RNase P probe: #10007062, RNase P primers: #10006837 and #10006836). Specimens were excluded based on their cycle thresholds (Ct) for RNase P, with those above 35 Ct being excluded due to insufficient quality for further analysis. N copy number was calculated based on linear regression of a standard curve with known N quantities.

Generation of KO primary bronchial epithelial cells. Cas9 ribonuclease complexes were complexed in vitro⁷⁰. Lyophilized tracrRNA (Horizon Discovery U-002005) & crRNA (Horizon Discovery, various, below) were resuspended to 160 µM, combined, and incubated at 37 °C for 30 min to form an RNA duplex at 80 µM. An equal volume of 40 µM Cas9-NLS protein solution (UCB Macrolab) was added and incubated at 37 °C for 15 min to produce crRNPs at 20 µM concentration. crRNPs were kept at -80 °C for storage or 4 °C for immediate use. Target sequences: DNAH5, AGACCCGAGAAAGATCTCGT (Horizon Discovery CM-009296-01); DNAI1, GATGAATACCGGGACCAGGT (Horizon Discovery CM-012419-02); CYPA, AGGTCCCCAAGA-CAGCAGGT (Horizon Discovery CM-004979-02); non-targeting: Horizon Discovery U-007503-01. Early passage bronchial epithelial cells were then trypsinized at 50–75% confluence, counted, separated into aliquots of 100,000 cells per reaction, and spun down at 200 × g × 5 min. Single reaction aliquots were then resuspended in 20 µL Lonza nucleofection buffer P3, mixed with 3.5 µL crRNP solution, placed in wells of a 16-well cuvette, and electroporated using program EH100 on a Lonza 4D X unit. Immediately after nucleofection, cells were mixed with 80 µL prewarmed Pneumacult Ex Plus medium and returned to the incubator for 30 min. Cells were then moved to collagen-coated 12-well plates with prewarmed Pneumacult Ex Plus medium and allowed to recover for approximately two days when the 12-well plates approached 70% confluence. At this point, cells were seeded on the underside of transwell membranes as described above.

Infection of ALI cultures. The mucus was removed from the apical surface of the culture by incubating with PBS for 30–45 min at 37 °C, then carefully removing residual mucus and PBS. Removal was performed either by aspiration or by use of Weck-Cel eye spears (Beaver-Visitec 0008680). The Weck-Cel method was less efficient at removing mucus and excess liquid, occasionally left autofluorescent debris, and was more likely to damage the epithelium. For these reasons, it was only used when aspiration was impermissible by BSL3 SOPs. For inverted cultures, 100 µL viral inoculum diluted in PBS to contain 5×10^5 PFU (~0.5 MOI) was placed in the bottom of a 24-well plate (Fisherbrand FB012929 or Greiner 662160) and ALI cultures placed on top such that the apical surface contacted the inoculum droplet. These plates have slightly shorter wells than the maintenance plates, enabling contact with low-volume inocula. For conventional cultures, 100 µL viral inoculum was pipetted onto the apical surface of the culture. Cultures were then incubated 1 h at warm room temperature (28 °C) with intermittent rocking. The apical surface was then rinsed twice with PBS and cultures were incubated at 37 °C with 5% CO₂. To quantify viral load in mucus, infected cultures were rinsed with PBS as prior to infection; residual mucus and PBS were carefully pipetted off and pooled with the remainder of the rinsate. Rinsate was stored at -80 °C until assayed by qPCR or plaque assay. For mucus qPCR, mucus samples were inactivated by heating to 60 °C for 30 min or 80 °C for 10 min as required by SOPs prior to analysis outside the BSL3 facility. For

immunofluorescence, cultures were inactivated and fixed by overnight or longer incubation at 4 °C in 4% formaldehyde in PIPES pH 6.8 buffer.

Agarose overlay. Prior to infection, 1% low melting temperature agarose (Invitrogen 16520) was melted on a heat block. After removal of the inoculum and PBS rinse as described above in the general infection protocol, residual PBS was thoroughly aspirated from the apical surface to ensure the agarose would have adequate contact with the culture to restrict mucus motion. 30 µL of melted agarose was spotted onto a clean surface and just prior to solidification, the freshly dried and infected transwell was stamped onto the spot to produce a thin layer of agarose over the apical surface.

Live imaging of ALI cultures. Live imaging was performed on a DeltaVision Elite microscope outfitted with stagetop incubator. Premixed blood gas was routed through an aquarium bubbler column filled with distilled water kept in the stagetop incubator to humidify and warm it to 37 °C, then piped onto cultures at 20 mL/min. Cultures were imaged in a glass-bottomed 24-well plate (Cellvis) with outer wells and interstitial spaces filled with distilled water to further maintain humidity and provide additional thermal mass. A 3D-printed adapter was used to fit the CO₂ frame lid to the 24-well plate. To mitigate condensation, the imaging cassette was equilibrated on the stage for at least 15 min prior to imaging and after any excursion to the hood. For movies of entire cultures, imaging was done in a 5 × 5 panel of 1024 × 1024 FOVs across 4 Z planes spanning 80 µm with a 4× air lens (Olympus UPLXAPO4X), with panels acquired every 2 h. For ciliary motion movies, 256 × 256 pixel FOVs were acquired with a 10× air lens at 125 frames per second. Centered on the smaller FOV of each ciliary motion video, 1024 × 1024 reference images of all channels spanning approximately 20 microns of Z were also acquired with the same 10× lens. For extended observation of individual infected cells, extreme caution was necessary to avoid moving cultures during media changes. Prior to imaging, cultures were stained with various dyes. Cellmask Orange Plasma membrane (Invitrogen C10045) was applied to the apical surface diluted 1:1000 in PBS for 7 min at 37 °C, then rinsed thrice with PBS. SPY650-tubulin (Spirochrome SC503) was mixed in the media at 1:2000 > 48 h prior to imaging and maintained in the media throughout. NucView 530 was mixed in the media at 1:500 shortly before initiation of imaging and maintained in media throughout except for in the ciliary motion knockout imaging when it was added two weeks prior. This mitigated the increase in background NV fluorescence seen in other experiments. Fluorescent beads (Invitrogen F8823 or F8807) were diluted in PBS and vortexed prior to addition to the apical surface in 2 µL volume.

Image processing: whole culture movies. Initial processing was performed in ImageJ. Panels were stitched using the Grid/Collection stitching plugin⁷¹. Stitched images were concatenated to assemble a full-time series, Z projected, and then registered using the Linear Stack Alignment with the SIFT Multichannel plugin to align across timepoints and media changes. Registered images were cropped prior to analysis, either manually or using the OpenCV implementation of the Hough circle transform. GFP+ spots were quantified using Trackmate 7 using a Laplacian of Gaussian spot detector³⁸. Rates of change of GFP+ spots were calculated in R based on fitted splines (spar = 0.1) to mitigate noise due to changes in the focal plane after media changes. Particle image velocimetry was performed using OpenPIV in Python to measure cell migration in cultures stained with SPY650-Tubulin. SPY650-tubulin coverage was calculated using a threshold set by the signal intensity in nascent beating cells in mid-differentiation ALI cultures.

Tracking of infected cells. For tracking without ciliary beat frequency measurements, single cells were simply followed from inception of the GFP signal to loss of signal in 4× magnification whole culture videos. Potential trackable cells were discarded from tracking if they became

impossible to discern from neighboring cells, or if they became part of an identifiable syncytium. For tracking with ciliary beat frequency measurements, 10x reference fields of view that were consistently acquired without excessive shifts over time were identified based on the SPY650-tubulin signal. The beat frequency of an infected cell was considered to be the median value in a region of interest drawn around the cell. All infected cells in a trackable field of view were measured. The matching region of the 4× magnification whole culture video was monitored in parallel to ensure correct tracking.

Qualitative whole culture image analysis. Qualitative assessments of mucociliary clearance, cell migration, crypt presence and morphology, and other culture parameters were made prior to observation of the GFP channel to avoid bias in these assessments. Organized or rotary mucociliary clearance was considered to consist of a single rotating disc of mucus which began rotating shortly after initiation of imaging; all other patterns were considered disorganized. Cultures where cell migration was observed in the center of the culture area or around the entire rim were considered to have widespread unjamming; cultures where cell migration was observed around part of the rim were considered to have edge unjamming; cultures where no cell migration was observed were described as jammed. In categorizing crypts, cysts were smaller bright SPY650-tubulin structures, either enclosed or with a pore; furrows were larger structures with epithelium folded over itself, either a single fold or multiple pleats.

Focus morphology was assessed after factors that might affect infection. Plaque-type foci were considered to be those that were dense, with many immediate neighboring cells infected, and potentially some trailing cells up to 4× plaque diameter. Comet-shaped foci had dense heads but longer tails than the plaque threshold, and generally a smooth transition between the dense focus head and the more diffuse tail area. Diffuse foci were those where the comet “tail” could not be delineated; dense seeding heads might be visible around the edges, but the shape of the focus is circular. Crypt foci were those where the infected cells lined up with whorls of the crypts. If a culture contained multiple types of foci, the type that covered the largest area was the dominant focus type.

Modeling of N RNA concentration of apical rinsates. Linear models incorporating combinations of the donor, percent ciliation, crypt, and cyst presence, jamming (categorically assigned or mean/median speed of cell migration), the extent of the presence of foci in crypts, and mucus motion pattern were assessed. Data from donors 5 & 6 were omitted due to multicollinearity. The model with the lowest Akaike information criterion was considered to be the best fit.

Statistics and Reproducibility. The significance of differences between pairs of distributions was calculated using two-tailed t-tests or Wilcoxon rank sum tests when normality assumptions were not met (assessed using the Shapiro test). Bonferroni corrections were applied where necessary to correct for multiple comparisons. For comparisons of multiple groups, we used one-way ANOVA followed by Tukey’s HSD.

Ciliary beat frequency measurement. 256 × 256 pixel videos of SPY650-tubulin cultures were acquired at an 8 ms framerate for 3 s using a 10× air lens. Videos were denoised using the generalist cytoplasm model from Cellpose3³¹. For each pixel, an FFT-based method (scipy.signal.periodogram) was used to assign a dominant frequency and a power associated with that frequency. Beat frequency images were then matched back to the corresponding position in Z-projected multichannel reference images. Code was written in Python.

MUC5AC dot blot. Apical rinsates from ALI cultures infected with SARS-CoV-2 WA1 were collected at various times, frozen at -80 °C, and inactivated at 80 °C for 10 min following SOPs. 3 µL inactivated rinsate was

spotted onto the nitrocellulose membrane (LI-COR 926-31092). After absorption, membranes were blocked for 1 h at room temperature (LI-COR 927-70001), then incubated overnight at 4 °C with anti-MUC5AC (Abcam 45M1) diluted 1:1000 in blocking buffer. After 3 × 5 min room temperature PBS-T 0.1% rinses, the membrane was incubated with secondary antibody (donkey anti-mouse IRDye 800CW, LI-COR 925-32212) diluted 1:20,000 in equal parts PBS and blocking buffer. After a final battery of rinses, the blot was imaged using a LICOR Odyssey imager.

Immunofluorescence. Uninfected cultures were fixed in 4% formaldehyde in pH 6.8 PIPES buffer at 4 °C overnight, then excised from the plastic transwell support and embedded in OCT. After cryo-sectioning onto superfrost slides, 10–12 µm sections were blocked with normal donkey serum and 0.5% Triton X for 45 min, then stained with primaries diluted in equal parts phosphate-buffered saline and blocking buffer. Primary incubations were all for 1 h at 37 °C. Anti acetyl alpha tubulin (Cell Signaling Technology D20G3, #5335, lot #4) was used at 1:800. Anti MUC5AC (45M1, Invitrogen MA5-12178, lot #YB37288), anti S (Sino 40150-D003, lot #MA14JU0501), anti ACE2 (Abcam ab15348, lot #GR333640-4), and anti TMPRSS2 (Abcam ab109131, lot #GR3248440-7) were used at 1:200. Anti dsRNA (rJ2, Sigma MABE1134, lot #3504410) was used at 1:1000 and anti N at 1:500 (Sino 40143-T62, lot #HD14JN0906-B). Donkey derived fluorescent secondaries (Jackson ImmunoResearch: Cy5 donkey anti-human #709-175-149, AF594 donkey anti-mouse #715-585-150, AF647 donkey anti-mouse #715-605-150, AF488 donkey anti-mouse #715-545-150, AF594 donkey anti-rabbit #711-585-152, AF488 donkey anti-rabbit #711-545-152, AF647 donkey anti-rabbit #711-605-152) with appropriate species specificity were diluted 1:500 in PBS and incubated on sections for 25 min at room temperature alongside Alexa Fluor™ 488 Phalloidin (Invitrogen A12379) where used. Slides were stained with Hoescht 33432 then mounted with Dako wet mount and sealed with nail polish. To mitigate section loss, staining was performed with an open-source derivative of the Sequenza coverslip staining platform. Slides were imaged on a DeltaVision Ultra or Elite widefield scope.

Reporting summary

Further information on research design is available in the Nature Portfolio Reporting Summary linked to this article.

Data availability

Summarized whole culture movie data and non-imaging data generated in this work are available in the Zenodo repository <https://doi.org/10.5281/zenodo.13892094>⁷². Source data for the figures are also provided with the paper. The live imaging data generated in this work are unviable for public hosting owing to their excessively large size (12.7 TB). Processed ciliary beat frequency data, a subset of raw ciliary beat frequency data, and a subset of processed whole culture movies have been deposited in Dryad under <https://doi.org/10.5061/dryad.7wm37pw0r>. Additional live imaging data, including raw and processed whole-culture movies and ciliary motion movies, are available upon request due to repository size limitations. Access to these data can be obtained by contacting Thomas Hope (thope@northwestern.edu) within 3 years of publication. Requests will be processed within 6 weeks, and if approved, arrangements will be made for data transfer via hard drives. Access is provided for research purposes and must comply with institutional data use agreements. Data will be available for a period of 5 years following the granting of access. Source data are provided with this paper.

Code availability

Code used for image processing and data analysis is available at https://github.com/markebecker/cov2_ali_imaging, <https://doi.org/10.5281/zenodo.13892094>⁷².

References

1. Hou, Y. J. et al. SARS-CoV-2 Reverse Genetics Reveals A Variable Infection Gradient In The Respiratory Tract. *Cell* **182**, 429–446.e14 (2020).
2. Killingley, B. et al. Safety, tolerability and viral kinetics during SARS-CoV-2 human challenge in young adults. *Nat. Med.* **28**, 1031–1041 (2022).
3. Zhou, J. et al. Viral emissions into the air and environment after SARS-CoV-2 human challenge: a phase 1, open label, first-in-human study. *Lancet Microbe* [https://doi.org/10.1016/s2666-5247\(23\)00101-5](https://doi.org/10.1016/s2666-5247(23)00101-5) (2023).
4. Knowles, M. R. & Boucher, R. C. Mucus clearance as a primary innate defense mechanism for mammalian airways. *J. Clin. Invest.* **109**, 571–577 (2002).
5. Zhang, L., Peebles, M. E., Boucher, R. C., Collins, P. L. & Pickles, R. J. Respiratory syncytial virus infection of human airway epithelial cells is polarized, specific to ciliated cells, and without obvious cytopathology. *J. Virol.* **76**, 5654–5666 (2002).
6. Chen, A. et al. Modeling insights into SARS-CoV-2 respiratory tract infections prior to immune protection. *Biophys. J.* **121**, 1619–1631 (2022).
7. Quirouette, C., Younis, N. P., Reddy, M. B. & Beauchemin, C. A. A. A mathematical model describing the localization and spread of influenza A virus infection within the human respiratory tract. *Plos Comput. Biol.* **16**, e1007705 (2020).
8. Wu, C.-T. et al. SARS-CoV-2 replication in airway epithelia requires motile cilia and microvillar reprogramming. *Cell* **186**, 112–130.e20 (2023).
9. Hill, D. B., Button, B., Rubinstein, M. & Boucher, R. C. Physiology and pathophysiology of human airway mucus. *Physiol. Rev.* **102**, 1757–1836 (2022).
10. Kamiya, Y. et al. Influenza A virus enhances ciliary activity and mucociliary clearance via TLR3 in airway epithelium. *Respir. Res.* **21**, 282 (2020).
11. Robinot, R. et al. SARS-CoV-2 infection induces the dedifferentiation of multiciliated cells and impairs mucociliary clearance. *Nat. Commun.* **12**, 4354 (2021).
12. Pittet, L. A., Hall-Stoodley, L., Rutkowski, M. R. & Harmsen, A. G. Influenza virus infection decreases tracheal mucociliary velocity and clearance of Streptococcus pneumoniae. *Am. J. Respir. Cell Mol. Biol.* **42**, 450–460 (2010).
13. Vijaykumar, K. et al. COVID-19 causes ciliary dysfunction as demonstrated by human intranasal micro-optical coherence tomography imaging. *Am. J. Respir. Cell Mol. Biol.* **69**, 592–595 (2023).
14. Li, Q. et al. Mucociliary transport deficiency and disease progression in Syrian hamsters with SARS-CoV-2 infection. *JCI Insight* **8**, e163962 (2023).
15. Schreiner, T. et al. SARS-CoV-2 infection dysregulates cilia and basal cell homeostasis in the respiratory epithelium of hamsters. *Int J. Mol. Sci.* **23**, 5124 (2022).
16. Zhu, N. et al. Morphogenesis and cytopathic effect of SARS-CoV-2 infection in human airway epithelial cells. *Nat. Commun.* **11**, 3910 (2020).
17. Morrison, C. B. et al. SARS-CoV-2 infection of airway cells causes intense viral and cell shedding, two spreading mechanisms affected by IL-13. *Proc. Natl Acad. Sci. USA* **119**, e2119680119 (2022).
18. Meyerholz, D. K. & Reznikov, L. R. Influence of SARS-CoV-2 on airway mucus production: a review and proposed model. *Vet. Pathol.* **59**, 578–585 (2022).
19. Michi, A. N. & Proud, D. A toolbox for studying respiratory viral infections using air-liquid interface cultures of human airway epithelial cells. *Am. J. Physiol. Lung Cell Mol. Physiol.* **321**, L263–L279 (2021).

20. Jonsdottir, H. R. & Dijkman, R. Coronaviruses and the human airway: a universal system for virus-host interaction studies. *Virol. J.* **13**, 24 (2016).
21. Cao, X. et al. Invited review: human air-liquid-interface organotypic airway tissue models derived from primary tracheobronchial epithelial cells—overview and perspectives. *Vitr. Cell. Dev. Biol. Anim.* **57**, 104–132 (2021).
22. Hao, S. et al. Long-term modeling of SARS-CoV-2 infection of in vitro cultured polarized human airway epithelium. *Mbio* **11**, e02852-20 (2020).
23. Thaler, M. et al. Impact of changes in human airway epithelial cellular composition and differentiation on SARS-CoV-2 infection biology. *J. Innate Immun.* <https://doi.org/10.1159/000530374> (2023).
24. Broadbent, L. et al. An endogenously activated antiviral state restricts SARS-CoV-2 infection in differentiated primary airway epithelial cells. *PLoS one* **17**, e0266412 (2022).
25. Ravindra, N. G. et al. Single-cell longitudinal analysis of SARS-CoV-2 infection in human airway epithelium identifies target cells, alterations in gene expression, and cell state changes. *PLoS Biol.* **19**, e3001143 (2021).
26. Martin-Sancho, L. et al. Functional landscape of SARS-CoV-2 cellular restriction. *Mol. Cell* **81**, 2656–2668.e8 (2021).
27. Matsui, H., Randell, S. H., Peretti, S. W., Davis, C. W. & Boucher, R. C. Coordinated clearance of periciliary liquid and mucus from airway surfaces. *J. Clin. Investigig.* **102**, 1125–1131 (1998).
28. Zaderer, V., Hermann, M., Lass-Flörl, C., Posch, W. & Wilflingseder, D. Turning the world upside-down in cellulose for improved culturing and imaging of respiratory challenges within a human 3D model. *Cells* **8**, 1292 (2019).
29. Bovard, D. et al. Comparison of the basic morphology and function of 3D lung epithelial cultures derived from several donors. *Curr. Res. Toxicol.* **1**, 56–69 (2020).
30. Khelloufi, M.-K. et al. Spatiotemporal organization of cilia drives multiscale mucus swirls in model human bronchial epithelium. *Sci. Rep.* **8**, 2447 (2018).
31. Stringer, C. & Pachitariu, M. Cellpose3: one-click image restoration for improved cellular segmentation. Preprint at *bioRxiv* <https://doi.org/10.1101/2024.02.10.579780> (2024).
32. Mitchel, J. A. et al. In primary airway epithelial cells, the unjamming transition is distinct from the epithelial-to-mesenchymal transition. *Nat. Commun.* **11**, 5053 (2020).
33. Spurlin, J. W. et al. Mesenchymal proteases and tissue fluidity remodel the extracellular matrix during airway epithelial branching in the embryonic avian lung. *Development* **146**, dev175257 (2019).
34. Stancil, I. T. et al. Interleukin-6-dependent epithelial fluidization initiates fibrotic lung remodeling. *Sci. Transl. Med.* **14**, eab05254 (2022).
35. Park, J.-A. et al. Unjamming and cell shape in the asthmatic airway epithelium. *Nat. Mater.* **14**, 1040–1048 (2015).
36. Tetley, R. J. et al. Tissue fluidity promotes epithelial wound healing. *Nat. Phys.* **15**, 1195–1203 (2019).
37. Mahlandt, E. K. & Goedhart, J. Fluorescent microscopy. *Methods Mol. Biol.* **2440**, 329–348 (2022).
38. Ershov, D. et al. TrackMate 7: integrating state-of-the-art segmentation algorithms into tracking pipelines. *Nat. Methods* **19**, 829–832 (2022).
39. Ye, C. et al. Analysis of SARS-CoV-2 infection dynamic in vivo using reporter-expressing viruses. *Proc. Natl Acad. Sci. USA* **118**, e211593118 (2021).
40. King, S. M. Axonemal dynein arms. *Cold Spring Harb. Perspect. Biol.* **8**, a028100 (2016).
41. Solomon, G. M. et al. Assessment of ciliary phenotype in primary ciliary dyskinesia by micro-optical coherence tomography. *JCI Insight* **2**, e91702 (2017).
42. Li, Y. et al. Global genetic analysis in mice unveils central role for cilia in congenital heart disease. *Nature* **521**, 520–524 (2015).
43. Eshel, D., Grossman, Y. & Priel, Z. Spectral characterization of ciliary beating: variations of frequency with time. *Am. J. Physiol. Cell Physiol.* **249**, C160–C165 (1985).
44. Hippee, C. E. et al. Measles virus exits human airway epithelia within dislodged metabolically active infectious centers. *PLoS Pathog.* **17**, e1009458 (2021).
45. Lin, W.-H. W., Tsay, A. J., Lalime, E. N., Pekosz, A. & Griffin, D. E. Primary differentiated respiratory epithelial cells respond to apical measles virus infection by shedding multinucleated giant cells. *Proc. Natl Acad. Sci. USA* **118**, e2013264118 (2021).
46. Zhang, L. et al. Infection of ciliated cells by human parainfluenza virus type 3 in an in vitro model of human airway epithelium. *J. Virol.* **79**, 1113–1124 (2005).
47. Gagliardi, T. B., Iverson, E., DeGrace, E. J., Rosenberg, B. R. & Scull, M. A. Immunofluorescence-mediated detection of respiratory virus infections in human airway epithelial cultures. *Curr. Protoc.* **2**, e453 (2022).
48. Thompson, C. I., Barclay, W. S., Zambon, M. C. & Pickles, R. J. Infection of human airway epithelium by human and avian strains of influenza A virus. *J. Virol.* **80**, 8060–8068 (2006).
49. Purkayastha, A. et al. Direct exposure to SARS-CoV-2 and cigarette smoke increases infection severity and alters the stem cell-derived airway repair response. *Cell Stem Cell* **27**, 869–875.e4 (2020).
50. Vahey, M. D. & Fletcher, D. A. Influenza A virus surface proteins are organized to help penetrate host mucus. *eLife* **8**, e43764 (2019).
51. Kosik, I. & Yewdell, J. W. Influenza hemagglutinin and neuraminidase: Yin-Yang proteins coevolving to thwart immunity. *Viruses* **11**, 346 (2019).
52. Iseli, A. N. et al. The neuraminidase activity of influenza A virus determines the strain-specific sensitivity to neutralization by respiratory mucus. *J. Virol.* **97**, e01271-23 (2023).
53. Kato, T. et al. Prevalence and mechanisms of mucus accumulation in COVID-19 lung disease. *Am. J. Respir. Crit. Care Med.* **206**, 1336–1352 (2022).
54. Hamele, C. E., Russell, A. B. & Heaton, N. S. In vivo profiling of individual multiciliated cells during acute influenza A virus infection. *J. Virol.* **96**, e00505–e00522 (2022).
55. Sun, J. et al. Single cell heterogeneity in influenza A virus gene expression shapes the innate antiviral response to infection. *PLoS Pathog.* **16**, e1008671 (2020).
56. Zhang, F. et al. Inhibition of major histocompatibility complex-I antigen presentation by sarbecovirus ORF7a proteins. *Proc. Natl Acad. Sci. USA* **119**, e2209042119 (2022).
57. Schaecher, S. R., Touchette, E., Schriewer, J., Buller, R. M. & Pekosz, A. Severe acute respiratory syndrome coronavirus gene 7 products contribute to virus-induced apoptosis. *J. Virol.* **81**, 11054–11068 (2007).
58. Tan, Y.-J. et al. Overexpression of 7a, a protein specifically encoded by the severe acute respiratory syndrome coronavirus, induces apoptosis via a caspase-dependent pathway. *J. Virol.* **78**, 14043–14047 (2004).
59. Taylor, J. K. et al. Severe acute respiratory syndrome coronavirus ORF7a inhibits bone marrow stromal antigen 2 virion tethering through a novel mechanism of glycosylation interference. *J. Virol.* **89**, 11820–11833 (2015).
60. Liu, Z. et al. Ubiquitination of SARS-CoV-2 ORF7a prevents cell death induced by recruiting BclXL to activate ER stress. *Microbiol. Spectr.* **10**, e01509–e01522 (2022).
61. Nemudryi, A. et al. SARS-CoV-2 genomic surveillance identifies naturally occurring truncation of ORF7a that limits immune suppression. *Cell Rep.* **35**, 109197 (2021).

62. Gangavarapu, K. et al. Outbreak.info genomic reports: scalable and dynamic surveillance of SARS-CoV-2 variants and mutations. *Nat. Methods* **20**, 512–522 (2023).
63. Abbasian, M. H. et al. Global landscape of SARS-CoV-2 mutations and conserved regions. *J. Transl. Med.* **21**, 152 (2023).
64. Burgel, P.-R. & Goss, C. COVID-19 outcomes in people with cystic fibrosis. *Curr. Opin. Pulm. Med.* **27**, 538–543 (2021).
65. Pedersen, E. S. L. et al. SARS-CoV-2 infections in people with primary ciliary dyskinesia: neither frequent, nor particularly severe. *Eur. Respir. J.* **58**, 2004548 (2021).
66. Erjefält, J. S., Erjefält, I., Sundler, F. & Persson, C. G. A. In vivo restitution of airway epithelium. *Cell Tissue Res.* **281**, 305–316 (1995).
67. Crosby, L. M. & Waters, C. M. Epithelial repair mechanisms in the lung. *Am. J. Physiol. Lung Cell. Mol. Physiol.* **298**, L715–L731 (2010).
68. Gudipaty, S. A. & Rosenblatt, J. Epithelial cell extrusion: pPathways and pathologies. *Semin. Cell Dev. Biol.* **67**, 132–140 (2017).
69. Levayer, R. Staying away from the breaking point: probing the limits of epithelial cell elimination. *Curr. Opin. Cell Biol.* **86**, 102316 (2024).
70. Hultquist, J. F. et al. CRISPR–Cas9 genome engineering of primary CD4+ T cells for the interrogation of HIV–host factor interactions. *Nat. Protoc.* **14**, 1–27 (2019).
71. Preibisch, S., Saalfeld, S. & Tomancak, P. Globally optimal stitching of tiled 3D microscopic image acquisitions. *Bioinformatics* **25**, 1463–1465 (2009).
72. Becker, M. E. et al. Live imaging of airway epithelium reveals that mucociliary clearance modulates SARS-CoV-2 spread, cov2_ali_imaging. Zemodo <https://doi.org/10.5281/zenodo.13892094> (2024).

Acknowledgements

We thank Ralph Baric & Luis Martinez-Sobrido for the reporter viruses. The following reagents were deposited by the Centers for Disease Control and Prevention and obtained through BEI Resources, NIAID, NIH: SARS-Related Coronavirus 2, Isolate hCoV-19/USA-WA1/2020, NR-52281, and SARS-Related Coronavirus 2, Isolate USA-WA1/2020, Recombinant Infectious Clone with Enhanced Green Fluorescent Protein (icSARS-CoV-2-eGFP), NR-54002. This research was supported, in part, through the computational resources and staff contributions provided by the Quest high-performance computing facility at Northwestern University, which is jointly supported by the Office of the Provost, the Office for Research, and Northwestern University Information Technology. Support was also provided by Northwestern University's BSL-3 Core Lab Facility with the help of Tiffany Johnson and James Zewe. Funding for this work was provided by: NIH grant R37 AI094595-09S1 (T.J.H.); NIH grant R21 AI163912 (J.F.H.); NIH grant U19 AI135964 (J.F.H.); NIH grant U19 AI135972 (S.K.C.); NIH grant U19 AI118610 (S.K.C.); and through institutional support for the Center for Pathogen Genomics and Microbial Evolution (J.F.H.). The funding sources had no role in the study design, data collection, analysis, interpretation, or writing of the report.

Author contributions

Conceptualization, M.E.B., J.F.H., T.J.H.; Methodology, L.M. Simons, M.E.B., M.D.M.; Software, M.E.B.; Validation, M.E.B.; Formal Analysis, L.M. Simons, M.E.B.; Investigation, L.M. Simons, L. Martin-Sancho, M.E.B.; Resources, J.F.H., T.J.H., M.D.M.; Data Curation, M.E.B.; Writing – Original Draft, M.E.B., J.F.H., T.J.H.; Writing – Review & Editing, M.E.B., J.F.H., T.J.H.; Visualization, M.E.B.; Supervision, J.F.H., S.K.C., T.J.H.; Project Administration, J.F.H., S.K.C., T.J.H.; Funding Acquisition, J.F.H., S.K.C., T.J.H.

Competing interests

J.F.H. has received research support, paid to Northwestern University, from Gilead Sciences and is a paid consultant for Merck. All other authors declare no conflicts of interest.

Additional information

Supplementary information The online version contains supplementary material available at <https://doi.org/10.1038/s41467-024-53791-4>.

Correspondence and requests for materials should be addressed to Thomas J. Hope.

Peer review information *Nature Communications* thanks Lisa Chakrabarti and the other anonymous reviewer(s) for their contribution to the peer review of this work. A peer review file is available.

Reprints and permissions information is available at <http://www.nature.com/reprints>

Publisher's note Springer Nature remains neutral with regard to jurisdictional claims in published maps and institutional affiliations.

Open Access This article is licensed under a Creative Commons Attribution-NonCommercial-NoDerivatives 4.0 International License, which permits any non-commercial use, sharing, distribution and reproduction in any medium or format, as long as you give appropriate credit to the original author(s) and the source, provide a link to the Creative Commons licence, and indicate if you modified the licensed material. You do not have permission under this licence to share adapted material derived from this article or parts of it. The images or other third party material in this article are included in the article's Creative Commons licence, unless indicated otherwise in a credit line to the material. If material is not included in the article's Creative Commons licence and your intended use is not permitted by statutory regulation or exceeds the permitted use, you will need to obtain permission directly from the copyright holder. To view a copy of this licence, visit <http://creativecommons.org/licenses/by-nc-nd/4.0/>.

© The Author(s) 2024